

# Steady shear rheology of a viscous emulsion in the presence of finite inertia at moderate volume fractions: sign reversal of normal stress differences

Priyesh Srivastava<sup>1</sup>, Abhilash Reddy Malipeddi<sup>2</sup> and Kausik Sarkar<sup>1,2,†</sup>

<sup>1</sup>Department of Mechanical Engineering, University of Delaware, Newark, DE 19716, USA

<sup>2</sup>Department of Mechanical and Aerospace Engineering, George Washington University, Washington, DC 20052, USA

(Received 12 June 2015; revised 8 August 2016; accepted 21 August 2016)

The shear rheology of an emulsion of viscous drops in the presence of finite inertia is investigated using direct numerical simulation. In the absence of inertia, emulsions display a non-Newtonian rheology with positive first and negative second normal stress differences. However, recently it was discovered that a small amount of drop-level inertia alters their signs – the first normal stress difference becomes negative and the second one becomes positive, each in a small range of capillary numbers (Li & Sarkar, *J. Rheol.*, vol. 49, 2005, pp. 1377–1394). Sign reversal was shown numerically and analytically, but only in the limit of a dilute emulsion where drop–drop interactions were neglected. Here, we compute the rheology of a density- and viscosity-matched emulsion, accounting for the interactions in the volume fraction range of 5%–27% and Reynolds number range of 0.1–10. The computed rheological properties (effective shear viscosity and first and second normal stress differences) in the Stokes limit match well with previous theoretical (Choi–Schowalter in the dilute limit) and simulated results (for concentrated systems) using the boundary element method. The two distinct components of the rheology arising from the interfacial stresses at the drop surface and the perturbative Reynolds stresses are investigated as functions of the drop Reynolds number, capillary number and volume fraction. The sign change is caused by the increasing drop inclination in the presence of inertia, which in turn directly affects the interfacial stresses. Increase of the volume fraction or capillary number increases the critical Reynolds number for sign reversals due to enhanced alignment of the drops with the flow directions. The effect of increasing the volume fraction on the rheology is explained by relating it to interactions and specifically to the contact pair-distribution function computed from the simulation. The excess stresses are seen to show an approximately linear behaviour with the Reynolds number in the range of 0.1–5, while with the capillary number and volume fraction, the variation is weakly quadratic.

**Key words:** drops and bubbles, emulsions, rheology

---

† Email address for correspondence: [sarkar@gwu.edu](mailto:sarkar@gwu.edu)

## 1. Introduction

Emulsions of immiscible liquids appear in many natural, biological and industrial phenomena. Their flows are determined by the microstructure of the constituting phases. The overall rheology connecting the flow properties to the coevolving microstructure has been extensively investigated and modelled (Tucker & Moldenaers 2002). However, previous studies neglected inertia in both the dispersed and the matrix phases. Recently, we investigated the effects of small drop-level inertia on a dilute emulsion of viscous drops and discovered that inertia can change the sign of the first and second normal stress differences (Li & Sarkar 2005*b*). Here, we extend that study to concentrated emulsions of moderate volume fractions. Through direct numerical simulation, we investigate how drop–drop interactions affect the steady shear rheology, in particular the anomalous sign change of the normal stress differences.

Research on the effective rheology of suspensions and emulsions has an illustrious history, starting with the seminal work of Einstein (1906). He predicted that the effective viscosity of a dilute rigid sphere suspension increases linearly with the volume fraction  $\phi$ , namely  $\mu_{effective} = \mu_m(1 + 2.5\phi)$ , where  $\mu_m$  is the viscosity of the suspending liquid. Taylor (1932) extended this to an emulsion of spherical viscous drops with a ratio  $\lambda$  of the drop to matrix viscosities:  $\mu_{effective} = \mu_m[1 + 2.5\phi(\lambda + 0.4)/(\lambda + 1)]$ . Using a perturbation method, Oldroyd (1953) obtained a linear Jeffrey-type viscoelastic constitutive equation for time varying flows with explicit expressions for the relaxation and retardation times (both proportional to the capillary time scale of the drop). Schowalter, Chaffey & Brenner (1968) were the first to consider the first-order effects of drop deformation on steady shear rheology, obtaining a positive first normal stress difference  $N_1$  and a negative second normal stress difference  $N_2$ , both proportional to  $\dot{\gamma}^2$ , square of the shear rate. Frankel & Acrivos (1970) generalized the result to obtain an expression for the stress tensor of an emulsion in time-dependent shear. All of the above investigations neglected interactions between drops, obtaining results of first order in the volume fraction  $\phi$ . A  $\phi^2$  correction to the expressions was obtained by Choi & Schowalter (1975), considering a cell model for interactions with neighbouring drops. The physics of the interaction between many drops beyond such perturbative analysis can only be investigated by numerical simulation.

It should be noted that in the one-particle dilute limit without any interactions, a rigid sphere suspension does not have any viscoelastic effect. Concentrated suspensions have been subjected to rigorous numerical investigation using Stokesian dynamics (Brady & Bossis 1988). This technique can accurately simulate hydrodynamic interactions between multiple particles, offering an excellent match between predictions and experimental observations. Interactions result in a viscoelastic behaviour with non-zero normal stress differences due to shear induced asymmetry in the particle distribution. Under different conditions, the effective viscoelasticity changes in the presence of hydrodynamic forces and interactions. At low Péclet numbers, where Brownian forces dominate the hydrodynamic forces, suspensions exhibit shear thinning, a positive first normal stress difference and a negative second normal stress difference. Strong hydrodynamic forces at higher Péclet number give rise to shear thickening due to the formation of hydrodynamic clusters and a negative first normal stress difference (Phung, Brady & Bossis 1996; Foss & Brady 2000).

In contrast to rigid particle suspensions, concentrated emulsions have attracted far fewer numerical simulations. Unlike their rigid counterparts, drops in an emulsion undergo deformation as well as coalescence and breakup, making such simulations

difficult. This partly explains the relative sparsity of the literature. Most simulations of emulsions, including the current study, do not account for coalescence or breakup. Zhou & Pozrikidis (1993) simulated two-dimensional random and periodic emulsions in a channel using the boundary element method (BEM). Loewenberg & Hinch (1996) used the same technique in three dimensions to simulate a concentrated emulsion in free shear and obtained the rheology – shear thinning, a positive first normal stress difference and a negative second normal stress difference. More recently, Zinchenko & Davis (2000) developed a highly accurate and efficient BEM algorithm, introducing multipole techniques that allowed simulations of  $\sim 100$  drops with  $\sim 1000$  nodes per drop. A larger number of drops was found to be necessary for accurate estimation of average properties for highly concentrated emulsions ( $>50\%$ ). For such systems, most of the shear thinning was found to occur sharply at the lowest capillary number (nearly non-deformed drops) (Zinchenko & Davis 2002, 2015).

Apart from direct numerical simulations, there have been semi-phenomenological approaches to modelling emulsion rheology using general physical features of the microstructure that can account for changes in structural topology arising from coalescence and breakup. Using the interface tensor that describes the effects of drop deformation on rheology first introduced by Batchelor (1970), Doi & Ohta (1991) developed a theory for a bicontinuous equal-viscosity blend. They offered a time evolution equation for the interface tensor, containing two additive tensorial contributions from capillary relaxation due to surface tension and flow mediated deformation. The model predicted a linear scaling for both the shear ( $\sigma_{12} \propto \dot{\gamma}$ ) and the first normal stress difference ( $N_1 \propto |\dot{\gamma}|$ ) (in contrast to  $N_1 \propto \dot{\gamma}^2$  in more conventional theory). The anomalous scaling stems from the kinematic origin of its length scale – droplet size proportional to  $1/\dot{\gamma}$  determined by coalescence and breakup – and has been observed experimentally (Takahashi *et al.* 1994; Vinckier, Moldenaers & Mewis 1996). However, the theory is inappropriate for blends with droplet-like microstructure, and has seen modifications to account for such effects (Lee & Park 1994; Peters, Hansen & Meijer 2001). Almusallam and coworkers (Almusallam, Larson & Solomon 2000) further improved the theory, including phenomenological ellipsoidal models for droplet shapes (Maffettone & Minale 1998; Wetzel & Tucker 2001; Jackson & Tucker 2003).

Investigation of the effective rheology of suspensions and emulsions has largely been restricted to inertialess Stokes flow. Lin, Peery & Showalter (1970) used an asymptotic technique to model the effects of finite particle level inertia on the rheology of a dilute rigid particle suspension, finding a negative first normal stress difference and a positive second normal stress difference. Patankar & Hu (2002) performed a two-dimensional simulation for the same system, finding again a negative first normal stress difference and a shear thickening behaviour. A two-dimensional lattice–Boltzmann (LBM) simulation of rigid sphere suspensions at finite inertia showed shear thickening and formation of clusters that increased initially with increasing Reynolds number before breaking up at larger inertia,  $Re \sim 10$  (Raiskinmaki *et al.* 2003). Morris and coworkers also used an LBM simulation and found the simulated normal stress differences to behave in accord with the analytical results of Lin *et al.* at low concentration ( $\phi < 0.1$ ) as functions of the particle concentration and Reynolds number (Kulkarni & Morris 2008; Haddadi & Morris 2014). However, for  $\phi \geq 0.2$  the second normal stress difference becomes negative at low  $Re$ . It should be noted that LBM simulation has also been used to compute the rheology of a similar but more complex system, namely a suspension of capsules enclosed by an elastic membrane (Clausen, Reasor & Aidun 2011). The authors noted that the

deformability of the capsules changes the sign of the first normal stress difference from negative – the same as for a rigid particle suspension – to positive – the same as for an emulsion of viscous drops – both in the Stokes limit.

As mentioned above, we have previously investigated dilute rheology (i.e. based on the flow field around a single drop) using a front-tracking method, predicting reversal of the signs of the normal stress differences with increasing Reynolds number (Li & Sarkar 2005*b*). This was followed up by a perturbative analysis by Subramaniam and coworkers (Raja, Subramaniam & Koch 2010; Subramaniam *et al.* 2011), providing an analytical confirmation of the sign reversal. This phenomenon stems from a purely geometric effect – a drop in shear reaches an inclination in excess of 45° with the flow direction at finite Reynolds number (Singh & Sarkar 2011). We also found negative normal stress elasticity in the effective oscillating extensional rheology (Li & Sarkar 2005*c,d*). These studies have, however, been limited to a dilute system, i.e. non-interacting drops. Here, we study the rheology of a concentrated emulsion with a moderate volume fraction (5–27%) in the presence of inertia, systematically varying the capillary number (0.02–0.2) and drop-scale Reynolds number (0.1–10). In the interest of brevity, we restrict the current study to a density- and viscosity-matched case, although the more general case does not pose any additional challenge for the computational methodology. A message passing interface (MPI) based parallel code incorporating a front-tracking algorithm (Bunner & Tryggvason 1999) is used for simulating this problem. The rheology, i.e. the effective stresses in the emulsion, is calculated using the stress formulation of Batchelor (1970).

## 2. Mathematical formulation

### 2.1. Governing equations and numerical formulation

The governing equations for the suspending liquid and the drops are the incompressible Navier–Stokes equations:

$$\left. \begin{aligned} \nabla \cdot \mathbf{u} &= 0, \\ \frac{\partial(\rho\mathbf{u})}{\partial t} + \nabla \cdot (\rho\mathbf{u}\mathbf{u}) &= -\nabla p + \nabla \cdot [\mu\{\nabla\mathbf{u} + (\nabla\mathbf{u})^T\}] - \int_{\partial B} \kappa \mathbf{n} \Gamma \delta(\mathbf{x} - \mathbf{x}') dS(\mathbf{x}'). \end{aligned} \right\} \quad (2.1)$$

In the above equations,  $\mathbf{u}$ ,  $p$ ,  $\rho$  and  $\mu$  represent the velocity, pressure, density and viscosity respectively,  $\kappa$  is the local drop surface curvature,  $\mathbf{n}$  is the unit outward normal to the surface  $\partial B$  of all drops and  $\Gamma$  is the interfacial tension. The equations are solved using a finite difference based front-tracking method (Bunner & Tryggvason 1999). It uses MPI libraries for parallel algorithm. The basic numerical method has been developed and used in many problems involving drops in viscous (Sarkar & Schowalter 2001; Li & Sarkar 2005*c,d*, 2006) and viscoelastic (Sarkar & Schowalter 2000; Aggarwal & Sarkar 2007, 2008*a,b*; Mukherjee & Sarkar 2010, 2011) media as well as capsules enclosed by an elastic membrane (Li & Sarkar 2008; Singh, Li & Sarkar 2014). Therefore, details will be spared here. Due to the explicit nature of the method, the time stepping of the simulation in the low-Reynolds-number cases here is severely restricted by the viscous time limit  $\Delta(t\dot{\gamma}) < Re\Delta(x/a)^2/6$ , which was partially alleviated by treating some of the viscous terms implicitly using an alternate direction implicit (ADI) scheme. It should be noted that the viscous capillary  $\Delta(t\dot{\gamma}) < Ca\Delta(x/a)$ , or inertia capillary  $\Delta(t\dot{\gamma}) < (CaRe)^{1/2}\Delta(x/a)^{3/2}$  (Brackbill, Kothe & Zemach 1992), considerations are less restrictive. The computational efficiency of this approach under the parallel methodology was verified. The reader is referred to

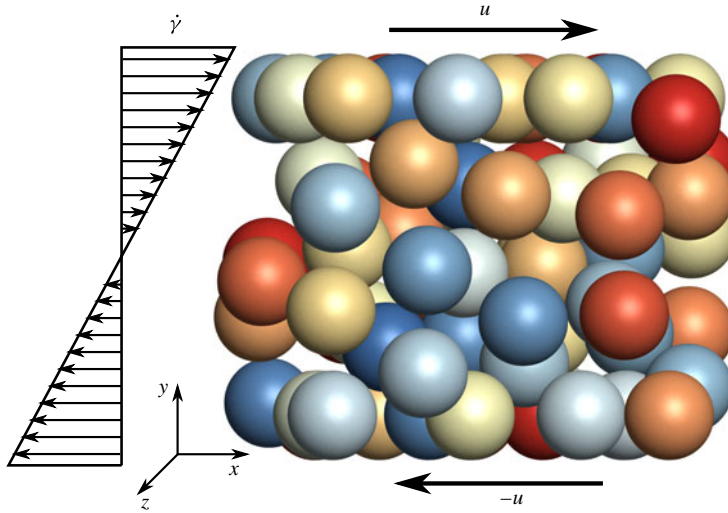


FIGURE 1. (Colour online) Schematic layout of the computational domain showing the random positions of the drops.

our previous articles (Sarkar & Schowalter 2001; Li & Sarkar 2005a) for further detail on the serial implementation.

The problem consists of multiple Newtonian drops initially all spherical with the same radius  $a$  suspended in a free shear. Computationally, the drops are placed in a domain of dimensions  $L_x \times L_y \times L_z$ . The effect of finite domain size is investigated. The upper and the bottom walls separated by a distance of  $L_y$  move with velocities  $+U$  and  $-U$  in the  $x$ -direction to simulate a uniform velocity gradient of  $\dot{\gamma} = 2U/L_y$  (figure 1). Periodic boundary conditions are applied in the flow ( $x$ ) and vorticity ( $z$ ) directions. By non-dimensionalizing the problem using the length scale  $a$  and the time scale  $\dot{\gamma}^{-1}$  one obtains several non-dimensional parameters: the Reynolds number  $Re = \rho \dot{\gamma} a^2 / \mu$  and the capillary number  $Ca = \mu \dot{\gamma} a / \Gamma$ . The viscosity and density ratios  $\lambda = \mu_d / \mu_m$  and  $\lambda_\rho = \rho_d / \rho_m$  between the drop and matrix phases are kept at unity here. The volume fraction of the emulsion is  $\phi = 4\pi a^3 N / 3V$ ;  $N$  is the number of drops suspended in the volume  $V = L_x \times L_y \times L_z$ . Most simulations, unless otherwise stated, are performed with domain dimensions the same in all directions,  $L_x = L_y = L_z = L$ , and therefore  $\phi = 4\pi N(a/L)^3/3$ .

Explicit computation of deforming drops at high concentration can lead to overlap of drops in close proximity. Zinchenko & Davis (2015) recently implemented a numerical procedure to prevent overlap and discussed how it extended the capabilities of their code and affected the results previously obtained without such a procedure (Zinchenko & Davis 2002). For the concentrations presented here, we did not encounter any difficulty due to overlap. It should also be noted that the smeared interface nature of the front-tracking code alleviates the computational problems in the event of overlap. The code will proceed, albeit with slight error, as the finite difference computation is not directly linked with the front; the front supplies the smeared forces due to the surface tension to the finite difference. The code was executed on the Mills cluster (200+ nodes with AMD6234 processors with 24/48 cores per node, 40 Gbps infiniband network-MPI) at the University of Delaware. Typical cases were simulated using 8, 16 or 64 processors depending on the availability on the cluster. A simulation

of 170 inverse shear unit takes 2 weeks on 64 processors and 27 days on 8 processors. However, the simulation duration may vary depending on the load on the system.

2.2. Effective bulk shear rheology

The bulk stresses of the emulsion are estimated using Batchelor’s formulation (Batchelor 1970), as was also done in our dilute rheology investigation (Li & Sarkar 2005b):

$$\begin{aligned}
 \sigma^{ave} &= \frac{1}{V} \int_V (\sigma - \rho \mathbf{u}'\mathbf{u}') dV \\
 &= -P_{ave} \mathbf{I} + \tau_{ave} + \frac{\mu_d - \mu}{V} \sum \int_{A_d} (\mathbf{u}\mathbf{n} + \mathbf{n}\mathbf{u}) dA \\
 &\quad - \frac{\Gamma}{V} \sum \int_{A_d} \left( \mathbf{n}\mathbf{n} - \frac{\mathbf{I}}{3} \right) dA - \frac{1}{V} \int_V \rho \mathbf{u}'\mathbf{u}' dV \\
 &= -P_{ave} \mathbf{I} + \tau_{ave} + \sigma^{excess},
 \end{aligned} \tag{2.2}$$

where

$$\left. \begin{aligned}
 \sigma^{excess} &= \sigma^{vrat} + \sigma^{int} + \sigma^{ptb}, \\
 \sigma^{vrat} &= \frac{\mu_d - \mu}{V} \sum \int_{A_d} (\mathbf{u}\mathbf{n} + \mathbf{n}\mathbf{u}) dA, \\
 \sigma^{int} &= -\frac{\Gamma}{V} \sum \int_{A_d} \left( \mathbf{n}\mathbf{n} - \frac{\mathbf{I}}{3} \right) dA, \\
 \sigma^{ptb} &= -\frac{1}{V} \int_V \rho \mathbf{u}'\mathbf{u}' dV.
 \end{aligned} \right\} \tag{2.3}$$

Here,  $V$  is the averaging volume (computational domain). It is assumed that the length scale of this volume is smaller than the macroscopic scale of the flow of the emulsion and is much larger than the size of the drops. The term  $A_d$  is the area of a drop and the summation is over all drops. The term  $P_{ave}$  is the average isotropic pressure and  $\tau_{ave}$  is the shear stress that would arise from the matrix if the drops were absent. Since the dispersing liquid is Newtonian, this term is easily obtained from its Newtonian constitutive relation. The term  $\sigma^{vrat}$  arising from the viscosity difference is zero for a viscosity-matched system, as is the case here. The term  $\sigma^{int}$  arises from the interfacial tension  $\Gamma$  at the drop interface. This is a purely geometric quantity determined by the instantaneous shapes of the drops. The term  $\sigma^{ptb}$  is a Reynolds stress type term; it represents the momentum fluxes due to the disturbances in the velocity field created by the presence of drops. The term  $\mathbf{u}' = \mathbf{u} - \bar{\mathbf{U}}$  is the perturbation velocity, and  $\bar{\mathbf{U}}$  is the mean velocity of the imposed shear flow. For the viscosity-matched system, these two terms represent the excess stress  $\sigma^{excess} = \sigma^{int} + \sigma^{ptb}$  due to the presence of drops. After computing them, the steady shear rheology of the emulsion will be characterized by the first normal stress difference  $N_1$ , the second normal stress difference  $N_2$  and the effective viscosity  $\mu_e$ :

$$\left. \begin{aligned}
 \frac{N_1}{\mu \dot{\gamma}} &= \frac{N_1^{excess}}{\mu \dot{\gamma}} = \frac{(\sigma_{xx}^{excess} - \sigma_{yy}^{excess})}{\mu \dot{\gamma}}, \\
 \frac{N_2}{\mu \dot{\gamma}} &= \frac{N_2^{excess}}{\mu \dot{\gamma}} = \frac{(\sigma_{yy}^{excess} - \sigma_{zz}^{excess})}{\mu \dot{\gamma}}, \\
 \frac{\mu_e}{\mu} &= 1 + \frac{\sigma_{xy}^{excess}}{\mu \dot{\gamma}} = 1 + \frac{\Sigma_{xy}^{excess}}{\mu \dot{\gamma}}.
 \end{aligned} \right\} \tag{2.4}$$

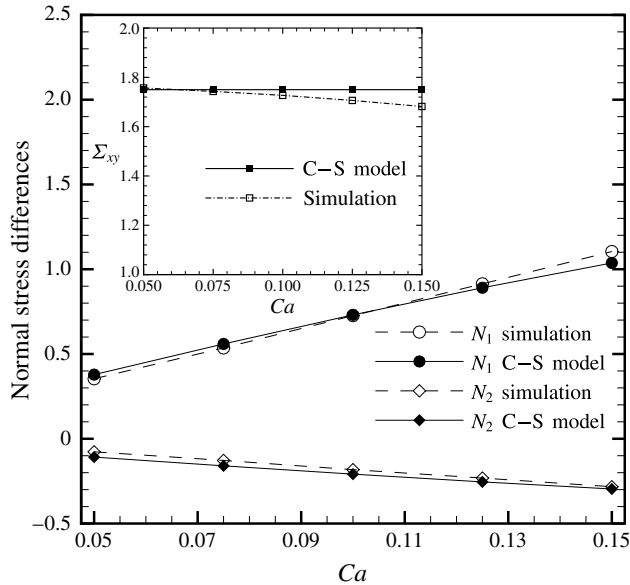


FIGURE 2. Comparison of the simulated effective stresses  $N_1, N_2$  and  $\Sigma_{xy}$  (inset) with the Choi–Schowalter model at  $\phi = 0.25\%$ ,  $Re = 0.1$ . The stresses are scaled by  $\mu\dot{\gamma}\phi$ .

We use the symbol  $\Sigma_{xy}$  for the excess shear stress, which is more common in the literature and was also used in our previous work (Li & Sarkar 2005b).

### 3. Results and discussion

#### 3.1. Dilute emulsion limit: comparison with the Choi–Schowalter model

We first consider a dilute emulsion with a volume fraction of  $\phi = 0.0025$  and compare the results with the Choi–Schowalter model (Choi & Schowalter 1975). The Choi–Schowalter model assumes Stokes flow; our simulations are performed at a small but non-zero value of the Reynolds number,  $Re = 0.1$ . The simulations are performed with four drops initially positioned at random locations in a domain of size  $15 \times 30 \times 15$  (normalized by the initial drop radius  $a$ ) with a grid resolution of  $128 \times 256 \times 128$ . This size is chosen to be sufficiently large (the effects of domain size on the results are examined in the next section). In figure 2, we plot the normal stress differences, the shear stress being plotted in the inset. The stresses have been scaled by  $\mu\dot{\gamma}\phi$ . The results are identical to what was observed in our previous dilute emulsion study using single drops (Li & Sarkar 2005b) – the normal stress differences match very well with the Choi–Schowalter model while the shear stress matches well at low capillary numbers. The deviation between the model and the simulation at higher  $Ca$  can be expected as the model is valid only for small deformation.

#### 3.2. Concentrated emulsion: numerical validation

In this paper, we investigate the rheology of an emulsion with varying capillary and Reynolds numbers in the volume fraction range of 5%–27%. The simulation involves a number of numerical parameters, e.g. the size of the domain (i.e. the averaging volume) relative to the drop size, the number of drops and the mesh resolution. In this section, we report on the sensitivity of the results to these parameters. It should

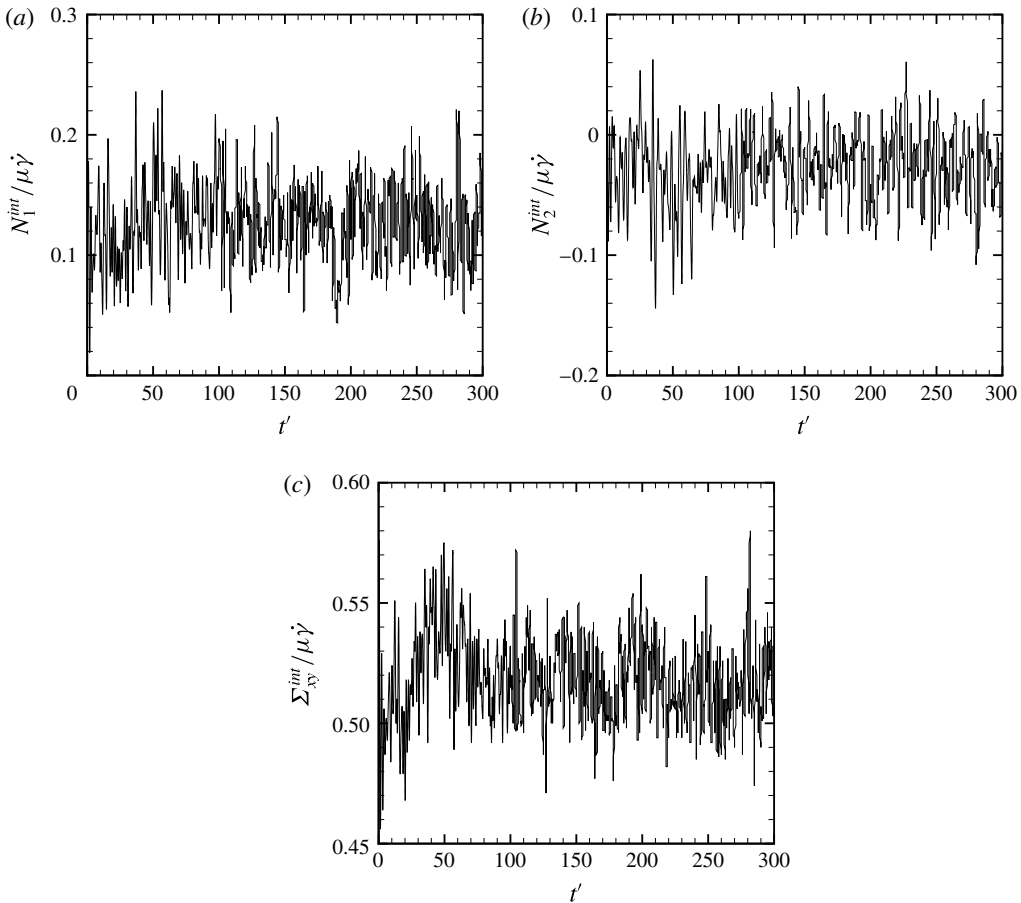


FIGURE 3. The time evolution of the effective interfacial stresses (a)  $N_1$ , (b)  $N_2$  and (c)  $\Sigma_{xy}$  ( $\phi=0.20$ ,  $Re=1.0$  and  $Ca=0.05$ , simulated using 64 drops and a  $128 \times 128 \times 128$  grid in an  $L \times L \times L$  domain).

be noted that the individual stresses, specifically the interfacial stresses arising from the drop shapes, fluctuate over time  $t'$  ( $=\dot{\gamma}t$ ) due to drop–drop interactions as drops come into close proximity to each other and separate (figure 3*a–c*). The rheological stresses discussed hereafter are obtained using time averaging after discarding an initial transient part of the simulation. The remaining portion of the simulation is subdivided into smaller time intervals (30 inverse shear units) and the average of each time interval is computed. These time interval averages are approximately uncorrelated (Zinchenko & Davis 2002). The mean of these averages is reported as the time averaged data (under the assumption of ergodicity, it is equal also to an ensemble average). The corresponding standard deviation of the averages of different time intervals is reported as the error below. The averages are obtained over a time evolution of at least 170 inverse shear units.

### 3.2.1. Grid resolution

We use an adaptive front surface regridting that controls front mesh distortion and the ratio of the front element length to the Eulerian grid spacing. The number of grid

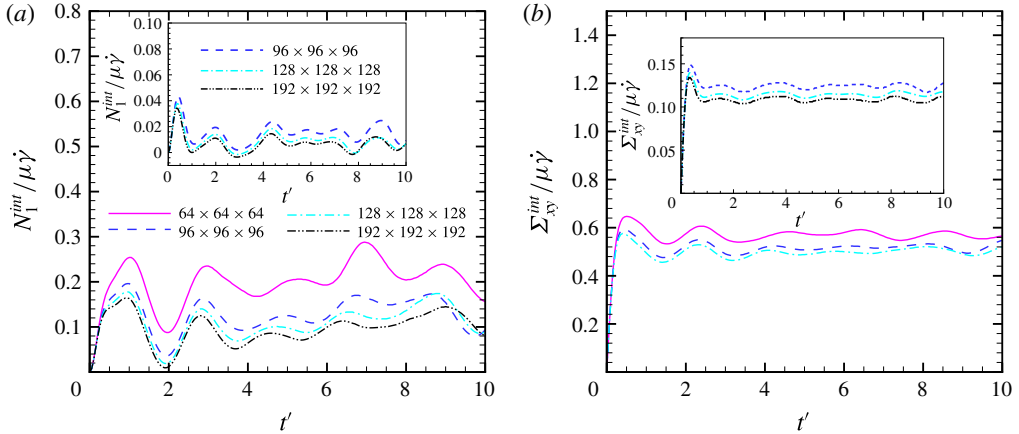


FIGURE 4. (Colour online) Variation of  $N_1^{int}$  (a) and  $\Sigma_{xy}^{int}$  (b) with grid resolution for  $\phi = 0.20$  at  $Ca = 0.05$  and  $Re = 1.0$  (the insets plot the same for  $\phi = 0.05$ ).

Grid resolution	$\Sigma_{xy}/\mu\dot{\gamma} (\times 10^{-1})$	$N_1/\mu\dot{\gamma} (\times 10^{-1})$	$N_2/\mu\dot{\gamma} (\times 10^{-2})$	Deformation ( $\times 10^{-1}$ )
$64 \times 64 \times 64$	$6.06 \pm 0.00481$	$2.21 \pm 0.0547$	$-6.74 \pm 0.4711$	$1.20 \pm 0.0307$
$96 \times 96 \times 96$	$5.59 \pm 0.00358$	$1.54 \pm 0.103$	$-4.96 \pm 0.706$	$1.11 \pm 0.0099$
$128 \times 128 \times 128$	$5.23 \pm 0.00702$	$1.33 \pm 0.0433$	$-3.22 \pm 0.851$	$0.996 \pm 0.0262$
$192 \times 192 \times 192$	$5.19 \pm 0.00223$	$1.17 \pm 0.0916$	$-3.13 \pm 0.502$	$0.989 \pm 0.0205$

TABLE 1. Grid resolution test at  $\phi = 20\%$ ,  $Re = 1.0$  and  $Ca = 0.05$ .

Grid resolution	$\Sigma_{xy}/\mu\dot{\gamma} (\times 10^{-1})$	$N_1/\mu\dot{\gamma} (\times 10^{-1})$	$N_2/\mu\dot{\gamma} (\times 10^{-1})$
$128 \times 128 \times 128$	4.11	5.12	-1.29
$192 \times 192 \times 192$	4.02	4.90	-1.23

TABLE 2. Grid resolution test at  $\phi = 20\%$ ,  $Re = 1.0$  and  $Ca = 0.20$ .

points in the Eulerian mesh therefore controls the overall grid resolution, specifically the ability of the mesh to resolve the surface tension force arising from the curvature of the drop interface. Figure 4(a,b) shows the effects of four different grids, namely  $64 \times 64 \times 64$ ,  $98 \times 98 \times 98$ ,  $128 \times 128 \times 128$  and  $192 \times 192 \times 192$  (for an  $L \times L \times L$  domain), on the time variations of the first normal stress difference and the shear stress at  $Ca = 0.05$ ,  $Re = 1.0$  and two different volume fractions,  $\phi = 5\%$  ( $L/a \sim 17$ ) and  $\phi = 20\%$  ( $L/a \sim 11$ ). The number of drops is  $N = 64$ . The results are plotted only for the first 10 time units, to avoid the clutter that would have resulted from the entire time range. However, the average values (time averages) are reported in the tables below. The simulations are averaged over at least 170 inverse shear units.

The data in tables 1–3 are computed by the method outlined before. Table 1 shows that the normal stress differences have sensitivity (the first normal stress the greatest) to the grid resolution while the shear stresses and deformations are relatively robust with less than 1% deviation at the maximum grid resolution of  $192 \times 192 \times 192$  from the smaller one of  $128 \times 128 \times 128$ . However, it should be noted that at this small value of the capillary number,  $Ca = 0.05$ , the deformation is small and therefore

Grid resolution	$\Sigma_{xy}/\mu\dot{\gamma}(\times 10^{-1})$	$N_1/\mu\dot{\gamma}(\times 10^{-2})$	$N_2/\mu\dot{\gamma}(\times 10^{-3})$	Deformation ( $\times 10^{-2}$ )
$96 \times 96 \times 96$	$1.21 \pm 0.00589$	$1.67 \pm 0.0654$	$4.63 \pm 0.517$	$8.32 \pm 0.0872$
$128 \times 128 \times 128$	$1.11 \pm 0.00755$	$1.07 \pm 0.0265$	$6.04 \pm 0.232$	$7.58 \pm 0.0821$
$192 \times 192 \times 192$	$1.06 \pm 0.00336$	$0.760 \pm 0.0442$	$7.06 \pm 0.442$	$7.05 \pm 0.0807$

TABLE 3. Grid resolution study at  $\phi = 5\%$ ,  $Re = 1.0$  and  $Ca = 0.05$ .

normal stresses are difficult to capture accurately. Table 2 shows that for  $Ca = 0.2$  the normal stresses have much less sensitivity (less than 5%) to grid variation. On the other hand, for the smaller volume fraction  $\phi = 5\%$  the drop sizes are smaller and therefore harder to accurately resolve, leading to some variation with grid size, as can be seen in table 3. However, we are more interested in higher concentrations (we investigate the  $\phi = 5\%$  case separately below). From the results presented in figure 4 and tables 1–3, we conclude that a grid size of  $128 \times 128 \times 128$  is sufficient for this study in the interest of maintaining a reasonable simulation time. The ranges of volume fraction and capillary number considered here are representative of the ranges that are used throughout the paper. Therefore, all simulations use this grid size (except at  $\phi = 5\%$ ).

### 3.2.2. Dependence on drop number variation and domain size

Zinchenko & Davis (2002) studied how the number of drops used for rheology calculation can be a source of both systematic and statistical errors. The statistical errors arise due to finite time averaging and can be decreased by averaging over longer time units so that a sufficient number of non-correlated drop interactions is captured. However, the systematic errors may persist due to finite domain size (periodic boundary conditions). They are further exacerbated due to the presence of the walls of the computational domain: a wall gives rise to wall induced migration of drops away from the wall (Chan & Leal 1981; Smart & Leighton 1991; Mukherjee & Sarkar 2013, 2014; Singh *et al.* 2014). Confinement by the two walls can also enhance the deformation and stabilize them, when they would otherwise break (Sibillo *et al.* 2006). The particular study by Sibillo *et al.*, however, focused on the case where the drop radius was comparable to the domain size, which can change the overall rheology. It should be noted that our aim here is the rheology in free shear. When sufficiently large numbers of drops are considered, the rheological properties should show little variation with further increase in drop number. Moreover, a large drop number ensures that their size relative to the wall separation remains small, minimizing the wall effects.

Table 4 shows the dependence of the interfacial and Reynolds stresses on the number of drops for a low capillary number of 0.05 and a Reynolds number of 1.0. This table shows that  $N = 16$  predicts a significantly higher  $N_1$  and lower  $\Sigma_{xy}$  than those at higher  $N$ . The average values of the stresses converge as the drop number is increased beyond 32 ( $\sim 5\%$ ). The value of  $L/a$  (i.e. wall separation to drop radius) is  $\sim 7$ –13 for the number of drops in the range  $N \sim 16$ –100. Table 4 suggests that  $N = 64$  is sufficient. It results in  $L/a = 11$ .

Fixing the number of drops at  $N = 64$ , but doubling the wall separation in the  $y$  direction, gives rise to a domain  $L \times 2L \times L$  ( $L/a = 9$ ) for the same volume fraction. Table 5 shows that doubling  $L_y$  causes very little change in  $\Sigma_{xy}$ . The value of  $N_2$  changes substantially, but then its value itself is quite small. We therefore use

Drops	$\Sigma_{xy}/\mu\dot{\gamma} (\times 10^{-1})$	$N_1/\mu\dot{\gamma} (\times 10^{-1})$	$N_2/\mu\dot{\gamma} (\times 10^{-2})$	$\sigma_{xx}^{pb}/\mu\dot{\gamma} (\times 10^{-2})$	$\sigma_{yy}^{pb}/\mu\dot{\gamma} (\times 10^{-2})$
16	4.795 ± 0.068	1.57 ± 0.22	-2.74 ± 1.1	5.64	2.34
32	5.097 ± 0.08	1.370 ± 0.089	-2.64 ± 0.37	6.48	2.76
64	5.23 ± 0.00702	1.33 ± 0.0433	-3.22 ± 0.851	6.26	2.91
100	5.264 ± 0.099	1.2564 ± 0.11	-2.997 ± 0.71	6.15	3.09

TABLE 4. Effects of number of drops at  $\phi = 20\%$ ,  $Re = 1.0$  and  $Ca = 0.05$ .

Domain size	$\Sigma_{xy}/\mu\dot{\gamma} (\times 10^{-1})$	$N_1/\mu\dot{\gamma} (\times 10^{-1})$	$N_2/\mu\dot{\gamma} (\times 10^{-2})$	$\sigma_{xx}^{pb}/\mu\dot{\gamma} (\times 10^{-2})$
$L \times L \times L (L/a = 11)$	5.23 ± 0.00702	1.33 ± 0.0433	-3.22 ± 0.851	6.26
$L \times 2L \times L (L/a = 9)$	5.10 ± 0.00616	1.17 ± 0.0602	-1.87 ± 0.371	6.92

TABLE 5. Effects of domain size at  $\phi = 20\%$ ,  $Re = 1.0$  and  $Ca = 0.05$ .

Drops	$\Sigma_{xy}/\mu\dot{\gamma} (\times 10^{-1})$	$N_1/\mu\dot{\gamma} (\times 10^{-1})$	$N_2/\mu\dot{\gamma} (\times 10^{-1})$
64	4.11 ± 0.0106	5.12 ± 0.0562	-1.29 ± 0.0662
100	4.21 ± 0.0146	5.40 ± 0.0405	-1.41 ± 0.0244

TABLE 6. Effects of number of drops at  $\phi = 20\%$ ,  $Re = 1.0$  and  $Ca = 0.20$ .

Drops	$\Sigma_{xy}/\mu\dot{\gamma} (\times 10^{-1})$	$N_1/\mu\dot{\gamma} (\times 10^{-2})$	$N_2/\mu\dot{\gamma} (\times 10^{-2})$
64	6.60	-2.02	7.63
100	6.73	-2.01	7.43

TABLE 7. Drop number study for  $\phi = 20\%$ ,  $Re = 5.0$  and  $Ca = 0.05$  (average values only).

$N = 64$  with the cubic domain with  $L/a = 11$  which we feel is adequate for the current purpose. Tables 6 and 7 show the effects of an increasing number of drops for different combinations of Reynolds and capillary numbers to further justify the choice  $N = 64$ .

Finally, we revisit the variation in the result with increasing grid size for the  $\phi = 5\%$  case seen in table 3 due to the relatively small drop size and therefore poor resolution at this small concentration. It should be noted that at such a small concentration, drops are sparsely populated and therefore a smaller number of drops in a fixed size domain (correspondingly higher resolution per drop) would be sufficient to describe the dynamics. The first three rows of table 8 show that an increase in drop number with a corresponding increase in grid points does not have a significant effect above  $N = 5$  for this case. The last three rows show that increase of the grid points beyond  $128 \times 128 \times 128$  while keeping the drop number fixed at  $N = 5$  also leads to little variation. We therefore use  $N = 5$  and  $128 \times 128 \times 128$  in all simulations for  $\phi = 5\%$  below.

### 3.2.3. Dependence on initial position variation

The rheology should be independent of the initial positions of the drops. This was investigated by fixing the volume fraction, Reynolds number and capillary number while varying the initial positions. Figure 5 compares the time evolution of the shear stress for two cases at  $\phi = 20\%$ ,  $Ca = 0.05$  and  $Re = 1.0$ . The first case corresponds

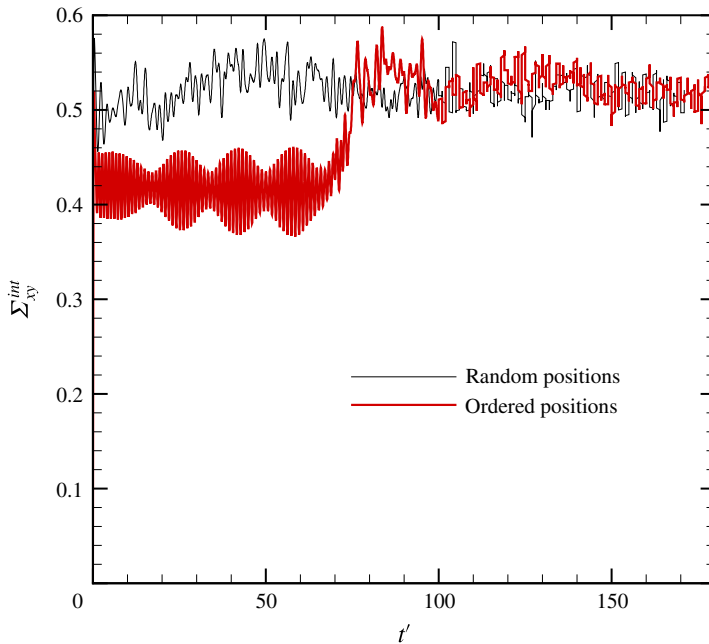


FIGURE 5. (Colour online) Effect of different initial positions on the development of shear stress ( $\phi = 0.20$ ,  $Re = 1.0$  and  $Ca = 0.05$ ).

Grid resolution, drops	$\Sigma_{xy}/\mu\dot{\gamma}$	$N_1/\mu\dot{\gamma}$	$N_2/\mu\dot{\gamma}$
$80 \times 80 \times 80$ , 1 drop	0.09628	0.009180	0.004681
$128 \times 128 \times 128$ , 5 drops	0.09547	0.004038	0.008006
$160 \times 160 \times 160$ , 10 drops	0.09548	0.002902	0.008840
$192 \times 192 \times 192$ , 20 drops	0.09805	0.002849	0.008861
$128 \times 128 \times 128$ , 5 drops	0.09547	0.004038	0.008006
$160 \times 160 \times 160$ , 5 drops	0.09492	0.004298	0.007686
$192 \times 192 \times 192$ , 5 drops	0.09540	0.004516	0.007443

TABLE 8. Grid resolution and drop number for  $\phi = 5\%$ ,  $Re = 1.0$  and  $Ca = 0.05$  (average values only).

to an initially ordered positioning of the drops and the second case corresponds to an initial random positioning. It is clear that the ordered system takes longer to break the initial structure. During the initial 70 time units, the drops move in layers (which is how they are initially distributed) for the ordered case. The shear stress is considerably low since the drop–drop interactions are minimal. After the structure breaks, interdrop interactions result in shear stresses close to those obtained from the second case. This illustrates two points. First of all, the stresses are independent of the initial configuration, as they should be. Second, for the simulation purposes, the initial positioning of the drops should be random to get good time averaged quantities in a reasonable number of cycles. For all simulations the drops are initially randomly positioned.

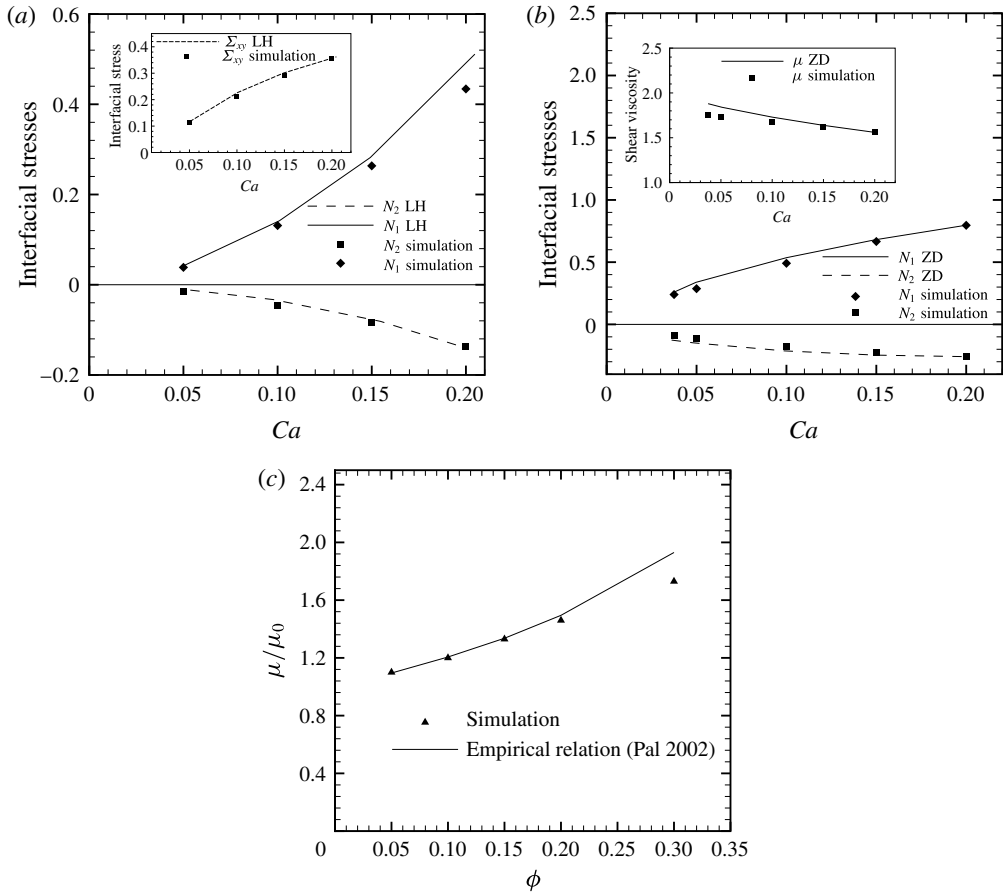


FIGURE 6. Comparisons of simulated  $N_1$ ,  $N_2$  and  $\Sigma_{xy}$  (inset) with BEM simulations of Loewenberg & Hinch (1996) (LH) at  $\phi = 20\%$  (a) and Zinchenko & Davis (2002) (ZD) at  $\phi = 30\%$  (b). Stresses are non-dimensionalized by  $\phi\Gamma/a$  in (a) and  $\mu\dot{\gamma}$  in (b). (c) Comparison of the viscosity versus volume fraction variation as predicted from simulation and empirical relations. Here,  $Re = 0.10$ ,  $Ca = 0.05$ .

### 3.3. Comparison with previous results of concentrated emulsion rheology

We compare our results (simulated at  $Re = 0.1$  to approximate Stokes flow) with those obtained using the BEM in the literature (Loewenberg & Hinch 1996; Zinchenko & Davis 2002) in figure 6(a,b). These two BEM results were for volume fractions of  $\phi = 20\%$  and  $\phi = 30\%$ . It should be noted that to facilitate comparison, stresses have been scaled by  $\phi\Gamma/a$  in figure 6(a) and by  $\mu\dot{\gamma}$  in figure 6(b). Our simulations match very well with the BEM except for at the low values of  $Ca$  in figure 6(b). It is interesting to note the difference – albeit slight (less than 4%) – between our result and that of Zinchenko & Davis (2002) for lower  $Ca$  values given that the two match very well at  $Ca = 0.15$  and  $0.2$ . At low capillary numbers (large value of surface tension), the drop deformation is small. Therefore, small deviations give rise to large variations in the purely geometric interfacial stress tensor that determines the interfacial stresses. The same authors (Zinchenko & Davis 2015) also noted the computational challenges of the system at small capillary numbers. Simulations

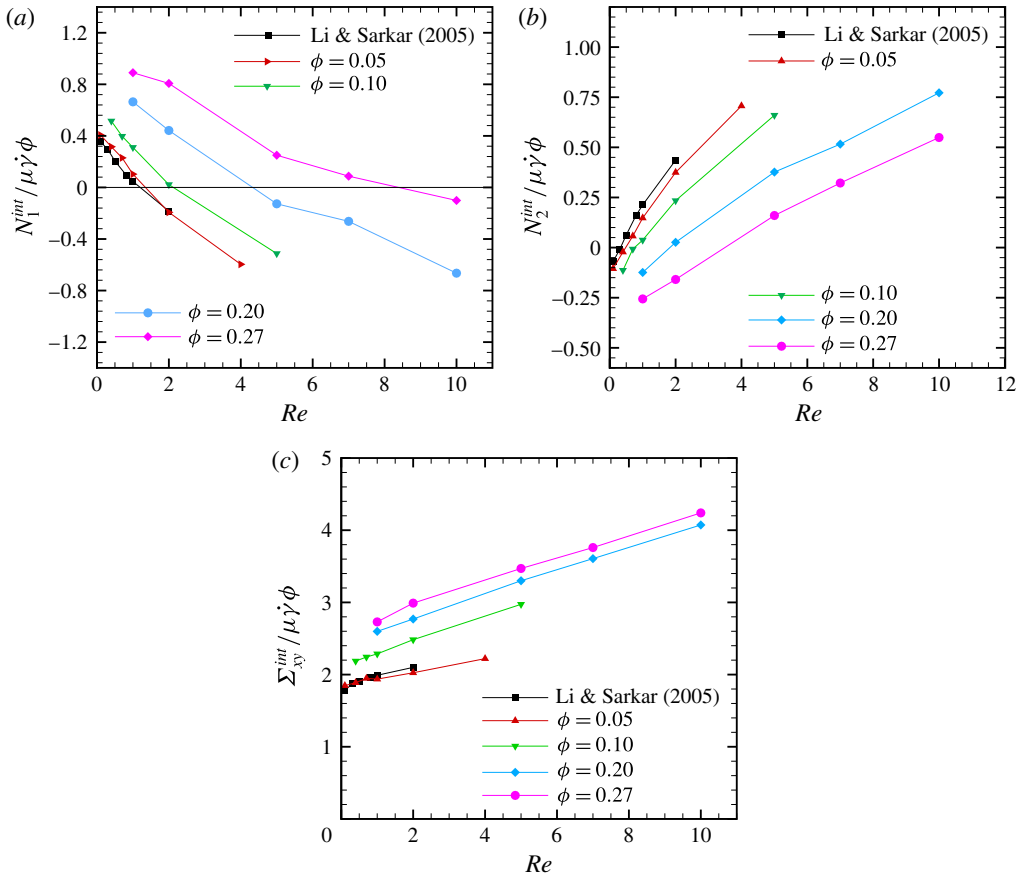


FIGURE 7. (Colour online) Variation of  $N_1^{int}$  (a),  $N_2^{int}$  (b) and  $\Sigma_{xy}^{int}$  (c) as functions of  $Re$ , all at  $Ca = 0.05$ .

performed in a larger domain and with an increased number of drops (128 drops in an  $L \times 2L \times L$  domain with  $128 \times 256 \times 128$ ) slightly improved the match with the BEM result at the lower capillary numbers. Figure 6(c) shows a comparison of the viscosity variation with volume fraction predicted by the simulation with the empirical relations obtained by Pal (2003). Pal derived three empirical models and tested them against a range of experiments. The third model in that paper was shown to give the best match with experiments. Figure 6(c) shows that the comparison with that empirical model is quite good.

### 3.4. Interfacial stresses $\sigma^{int}$ : effects of $Re$ and volume fraction

It should be noted that according to (2.3), the effective stresses for the viscosity-matched system have two contributions  $\sigma^{int}$  and  $\sigma^{ptb}$ . The second component arises as a direct effect of finite inertia and increases with increasing Reynolds number. We found earlier (Li & Sarkar 2005b) that  $\sigma^{int}$  is much larger in magnitude than  $\sigma^{ptb}$  in the dilute emulsion limit for low Reynolds numbers ( $Re \leq 1$ ). Figure 7(a–c) shows the dependence of the interfacial stresses  $\sigma^{int}$  on the Reynolds number for four different volume fractions. The plots also include the dilute emulsion results

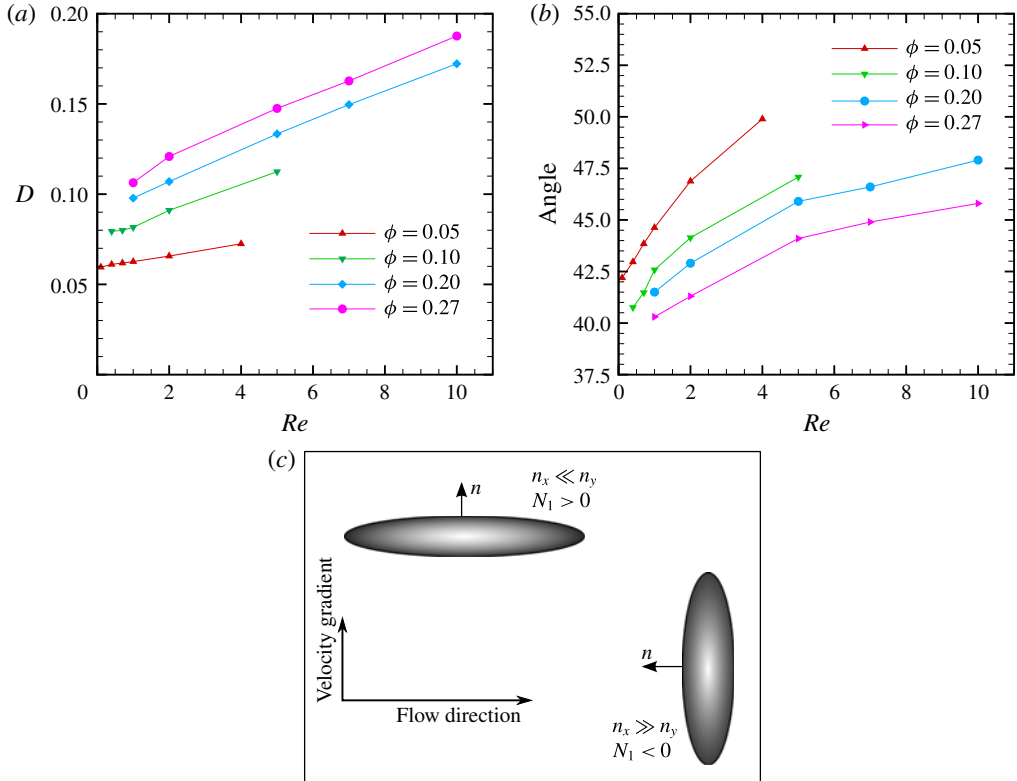


FIGURE 8. (Colour online) Variation of drop inclination (a) and deformation (b) as functions of  $Re$ , both at  $Ca = 0.05$ . (c) Sketch of drop orientations.

of Li & Sarkar (2005b) where the sign reversal of the normal stress differences with Reynolds number was first noticed. The stresses have been scaled by  $\phi$  to allow comparison between different volume fractions. The capillary number is fixed at 0.05. These plots show that  $N_1^{int}$  decreases while  $N_2^{int}$  increases with Reynolds number in the entire range of volume fractions considered here, leading eventually to reversal of their signs (Li & Sarkar 2005b). It should be noted that although scaled by  $\phi$ , the curves for different volume fractions do not collapse onto a single curve, indicating nonlinear dependence on  $\phi$  of the interparticle interactions – pair, triple and higher-order interactions (Zhou & Pozrikidis 1993). Increasing volume fraction delays the reversal of signs of the interfacial normal stress differences. The interfacial shear stress increases with Reynolds number over the volume fraction range considered.

The above observations can be explained by considering the average drop orientation and deformation. As noted before,  $\sigma^{int}$  is determined by the geometry of the drop (see (2.3)). Previously, we demonstrated that the sign reversal of the first normal stress difference occurs due to the drop inclination becoming greater than  $45^\circ$  with increasing inertia (Li & Sarkar 2005b; Singh & Sarkar 2011). Here, we provide a simple physical explanation of the phenomenon. We plot the average drop deformation and angle of inclination as functions of  $Re$  for various volume fractions in figure 8(a,b). The average deformation increases with increasing volume fraction while the inclination decreases. It should be noted that the normal stress differences

consist of an additive contribution from each drop of the  $N$  drops present:

$$\left. \begin{aligned} N_1^{int} &= \sigma_{xx}^{int} - \sigma_{yy}^{int} \sim -N \int_{\delta A} (n_x^2 - n_y^2) dA, \\ N_2^{int} &= \sigma_{yy}^{int} - \sigma_{zz}^{int} \sim -N \int_{\delta A} (n_y^2 - n_z^2) dA. \end{aligned} \right\} \quad (3.1)$$

Figure 8(c) shows two extreme orientations of a drop relative to the flow direction. If the drop is aligned along the flow ( $x$ ) direction then  $n_x \ll n_y$  for most of the surface, leading to  $N_1 > 0$  according to (3.1). On the other hand, if the drop is aligned along the velocity gradient,  $N_1 < 0$ . If the drop is aligned along the extensional axis, i.e. with an inclination angle of  $45^\circ$ ,  $N_1 \approx 0$ . An inclination angle in excess of  $45^\circ$  changes the sign. A similar argument can also be given for  $N_2$ . Typically, for orientation along the flow direction, dominance of  $n_y$  gives rise to  $N_2 < 0$ . As the drop rotates in its shear plane from the flow direction to the velocity gradient direction,  $n_y$  decreases but  $n_z$  remains roughly unchanged. It increases  $N_2$ , eventually making it positive. The total interfacial stress is dictated by drop inclination averaged over all drops. Similar to the case of a single drop in shear (Li & Sarkar 2005b), figure 8(b) here shows that the average drop inclination increases with Reynolds number, eventually exceeding  $45^\circ$ , leading to the sign reversal of  $N_1$ . It should also be noted that the average drop inclination decreases with increasing volume fraction because of the aligning influence from flowing drops in the neighbourhood, as was also noted before in Stokes flow (Loewenberg & Hinch 1996). It delays the sign reversal seen in figure 7(a,b).

Figure 7(c) shows that the effective shear stress increases with Reynolds number at a fixed volume fraction. It also increases with volume fraction at a fixed Reynolds number. Similar to (3.1), the individual contribution from a drop towards the average interfacial shear stress is

$$\Sigma_{xy}^{int} \sim - \int_{\delta A} n_x n_y dA. \quad (3.2)$$

However, the cross-term does not render an easy explanation of the increase of shear stress with  $Re$  in terms of the inclination angle. For an ellipsoidal drop, one can compute the geometric integral in terms of an elliptic integral (Almusallam *et al.* 2000). A simpler expression, assuming a drop shape of a capped short cylinder, is provided by Loewenberg & Hinch (1996):

$$\Sigma_{xy}^{int} \approx \sin(2\theta)D. \quad (3.3)$$

Here,  $D$  is the Taylor deformation ( $L$  and  $B$  are the major and minor axes respectively of the deformed drop,  $D = (L - B)/(L + B)$ ). This expression shows the combined effects of the deformation and inclination. With increasing inertia, the deformation and inclination increase. The inclination term  $\sin 2\theta$  increases or decreases to  $\sim \pm 0.98$  from its maximum value of 1.0 at  $\theta = 45^\circ$  when changed by  $\pm 5^\circ$  (figure 8b). However, figure 8(a) shows that the deformation  $D$  increases twofold over the range of  $Re = 1-10$ , leading to the observed enhancement in shear stress. Increasing deformation with volume fraction also explains the increasing shear stress with volume fraction.

### 3.5. Interfacial stresses $\sigma^{int}$ : effects of $Re$ and $Ca$

For a single drop, we have shown that the inclination angle increases with increasing Reynolds number for smaller capillary numbers; at higher capillary numbers, the

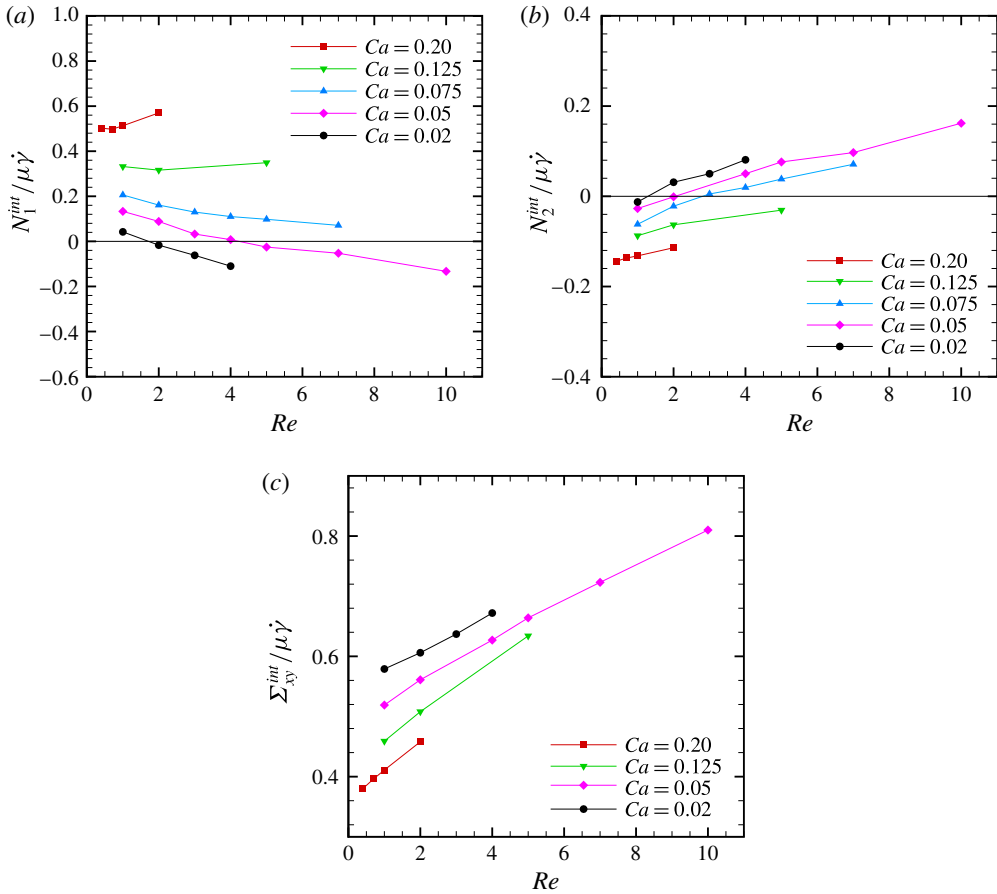


FIGURE 9. (Colour online) Variation of interfacial stresses with  $Re$  for different  $Ca$ : (a)  $N_1^{int}$ , (b)  $N_2^{int}$  and (c)  $\Sigma_{xy}^{int}$  at  $\phi = 20\%$ .

increased deformation at higher inertia leads to an eventual decrease of inclination with increasing inertia (Singh & Sarkar 2011). The drop inclination changes and thereby the sign reversal could alternately be described by the Ohnesorge number – the ratio between the Reynolds and capillary numbers (Raja *et al.* 2010). The sign reversal of normal stress differences appears at a critical Ohnesorge number and the phenomenon is seen in a small range of capillary numbers (Li & Sarkar 2005*b*). We first investigate in figure 9 variations of the interfacial normal stress differences and shear stress with Reynolds number over a range of capillary numbers at a fixed volume fraction of 20%. Figure 9(a) shows that the sign reversal of  $N_1^{int}$  occurs for the lowest two capillary numbers ( $Ca = 0.02$  and  $0.05$ ), and takes place at a lower Reynolds number for the smaller  $Ca$ . For the other  $Ca$  values ( $>0.05$ ),  $N_1^{int}$  decreases with increasing inertia at least initially but does not become negative. The drop experiences large deformation, leading to eventual breakup beyond  $Re = 5$  at  $Ca = 0.125$  and  $Re = 2$  at  $Ca = 0.2$ . Similar variation and sign reversal (delayed at higher  $Ca$ ) of  $N_2^{int}$  are observed in figure 9(b). With increasing  $Re$ , the shear stress  $\Sigma_{xy}^{int}$  increases due to increased deformation (figure 9c). From figures 7(a–c) and 9(a–c)

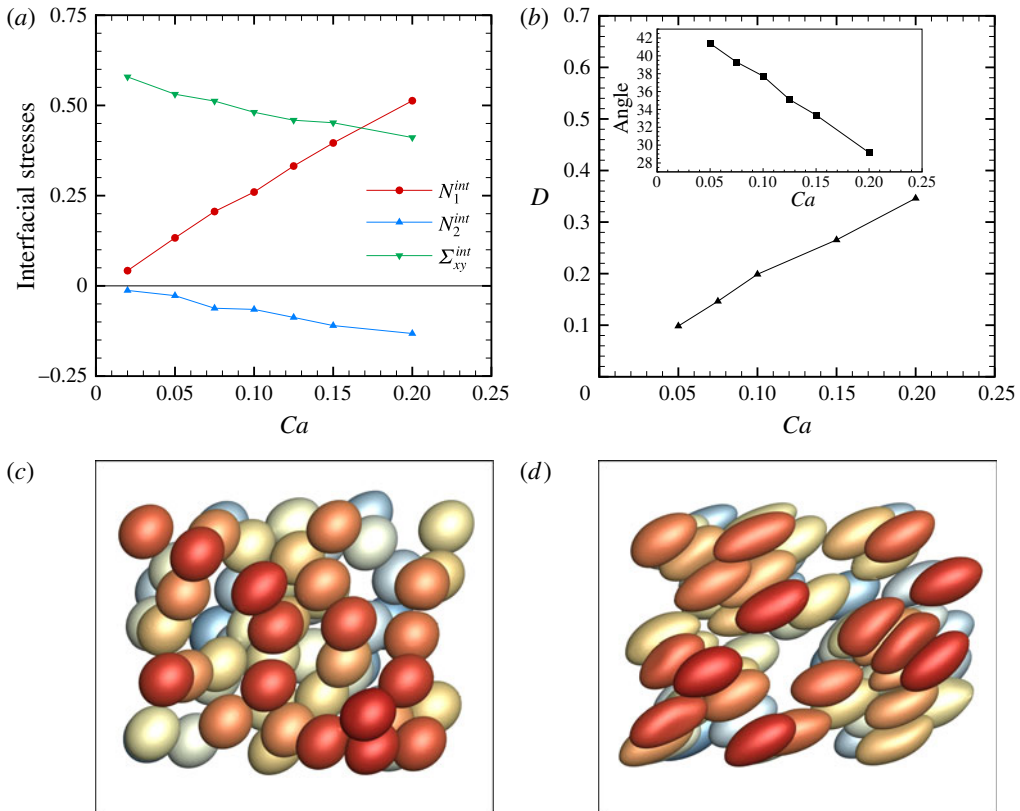


FIGURE 10. (Colour online) Variation of interfacial stresses non-dimensionalized by  $\mu\dot{\gamma}$  (a), deformation and inclination angle (b) with  $Ca$  at  $Re = 1.0$  and  $\phi = 20\%$ . Drop shapes at  $Ca = 0.05$  (c) and  $Ca = 0.2$  (d), both for  $Re = 1.0$  and  $\phi = 20\%$ .

one can see an approximately linear variation of the normal stress differences and the shear stress with  $Re$ , at least for the lower capillary numbers.

Figure 10(a,b) shows the dependence of the interfacial stresses, the deformation and the inclination on the capillary number at fixed Reynolds number ( $Re = 1.0$ ) and volume fraction ( $\phi = 20\%$ ). With increasing capillary number,  $N_1^{int}$  increases linearly, while  $N_2^{int}$  and  $\Sigma_{xy}^{int}$  linearly decrease. Decreasing shear stress with increasing shear rate – shear thinning – is well known and can be attributed to the precipitous decrease in inclination (figure 10b inset) and relation (3.3). The increased deformation and the resulting decreased inclination at larger  $Ca$  can also be seen in figure 10(c,d). Corresponding effects on the surface normal components  $n_x$  and  $n_y$  explain the behaviour of  $N_1^{int}$  and  $N_2^{int}$  as per equation (3.1). The shear thinning behaviour and the increase in the first normal stress difference were measured experimentally by Han & King (1980), and seen in simulation by Loewenberg & Hinch (1996). It should also be noted that the fact that the non-dimensional normal stresses  $N_{1,2}/\mu\dot{\gamma}$  are linear with  $Ca = \mu\dot{\gamma}a/\Gamma$  is in agreement with the well-known relation  $N_{1,2} \propto \dot{\gamma}^2$  for small shear rates. The quadratic variation with shear rate motivates the definition of normal stress coefficients  $\Psi_{1,2} = N_{1,2}/\dot{\gamma}^2$  often used in the literature (Larson 1999).

Loewenberg & Hinch (1996) observed that the shear viscosity contribution of drops increases with volume fraction at lower shear rates, remains independent of

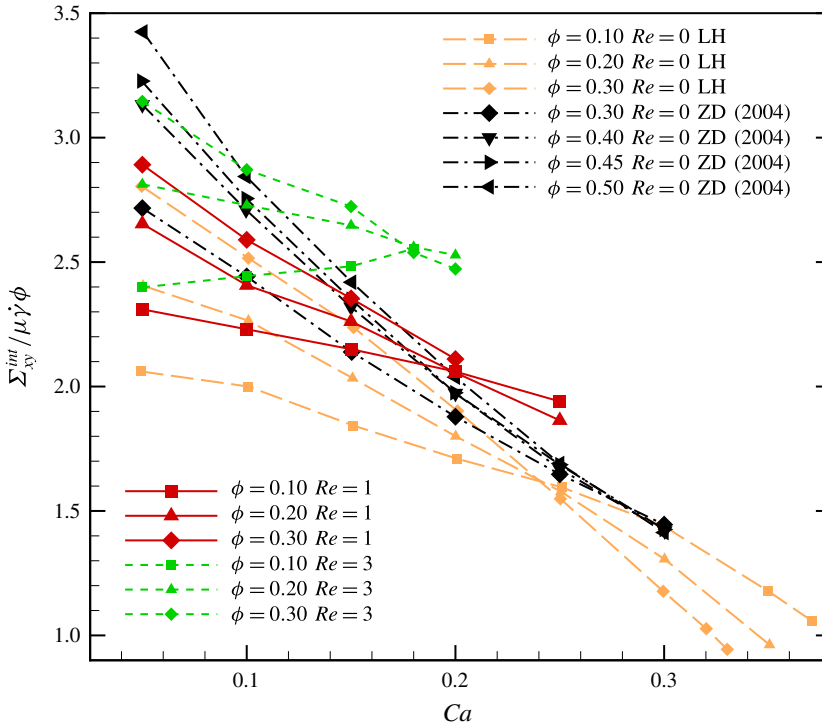


FIGURE 11. (Colour online) Interfacial viscous stress contribution due to drops as a function of  $Ca$  for different volume fractions and different values of  $Re$ . The ‘cross-over/convergence’ capillary number decreases with increasing  $Re$ . Here, LH and ZD (2004) refer to the BEM simulations by Loewenberg & Hinch (1996) and Zinchenko & Davis (2004) respectively.

volume fraction at  $Ca = 0.25$ , and decreases with volume fraction at higher shear rates ( $Ca > 0.25$ ). These authors argued that at lower capillary numbers, the increase in viscosity with volume fraction arises from increasing drop collisions. At higher capillary numbers, drops experience larger deformation; increased interactions at increasing volume fraction align them with the flow (decreased inclination), which in turn leads to decreasing viscosity (with increasing volume fraction). The authors found the viscosity versus  $Ca$  curves for different volume fractions to cross over at  $Ca = 0.25$ . More accurate BEM computations by Zinchenko & Davis (2004) found the convergence of the viscosity versus  $Ca$  curves for different volume fractions to occur at a higher  $Ca$  value. We investigate how inertia affects this phenomenon, including both results for Stokes flow in figure 11. The capillary number for convergence decreases with Reynolds number. At higher Reynolds numbers, simulation of larger-capillary-number cases could not be continued due to eventual breakup of drops. It should be noted that for  $Re = 3$ , at the lowest concentration of  $\phi = 10\%$ , the viscosity contribution increases with capillary number in contrast to all other cases seen here as well as in figure 10. This can be explained by equation (3.3) in view of the increased deformation and enhanced drop inclination at this higher  $Re$  value. At higher volume fractions, drop–drop interactions decrease the inclination, reversing this effect. A reversal of trend in shear viscosity with capillary number – decreasing at lower  $Re$  and increasing at higher  $Re$  – was also observed for dilute emulsions (Li & Sarkar 2005b).

### 3.6. Drop–drop interactions and pair-distribution function in concentrated emulsions

Thus far, we have explained rheological observations in terms of the individual drop response. With increasing emulsion concentration, drop–drop interactions become progressively more important. However, it should be noted that the general relation for effective stresses involves individual drop contributions:

$$\sigma^{int} = -\frac{\Gamma}{V} \sum \int_{A_d} \left( \mathbf{nn} - \frac{\mathbf{I}}{3} \right) dA = \sum_1^N \mathbf{S}_{ij} = N \bar{\mathbf{S}}_{ij}. \quad (3.4)$$

Here,  $\mathbf{S}_{ij}$  is the traceless stresslet tensor and  $\bar{\mathbf{S}}_{ij}$  is the stresslet averaged over all of the drops. Drop–drop interactions modify the individual drop contributions. To understand the effects of interactions on the emulsion rheology, we note that following (Batchelor & Green 1972), the average stresslet can be written as

$$\bar{\mathbf{S}}_{ij} = \mathbf{S}_{ij}^\circ + \int P(X) \Delta \mathbf{S}_{ij} dX. \quad (3.5)$$

The first term in the right-hand side is the single-drop stresslet under the given hydrodynamic conditions and does not include the effects of interdrop interactions. The second term represents the additional contribution to the stresslet  $\Delta \mathbf{S}_{ij}$  due to interactions for a particular relative configuration  $X$  with probability  $P(X)$ ; this term is averaged over all possible relative configurations. This term can be approximated by only considering the probability of two drops closely interacting in their shear plane using the pair-distribution function at contact. The pair-distribution function  $g(\mathbf{r})$ , the probability of finding a second particle at a relative distance  $\mathbf{r}$  from any particle, has been extensively analysed in suspension rheology (Phung *et al.* 1996; Brady & Morris 1997; Morris & Katyal 2002; Clausen *et al.* 2011). Specifically, its value at contact, i.e. for two particles nearly touching each other, as a function of the orientation of the particle pair is used to explain the observed non-Newtonian behaviour of rigid sphere suspensions.

Figure 12(a,b) plots the pair-distribution probability as a function of the azimuthal angle of a drop in the shear plane – from the direction of approach of a second drop (near  $180^\circ$ ), through the compression quadrant, to where the second drop separates away (near  $0^\circ$ ). For deformable drops, the contact pair-distribution function is defined here by limiting the distances between two drops to the range of  $1.5a$ – $2.4a$  ( $a$  is the drop radius). The probability is highest in the compression quadrant and near zero away in the extension quadrant especially during separation. During the time when drops are pressed in the compression quadrant, their deformation increases (Loewenberg & Hinch 1997; Olapade, Singh & Sarkar 2009; Singh & Sarkar 2009), increasing the stresslet contribution. Figure 12(a) plots the pair-distribution probability for one capillary number,  $Ca = 0.05$ , and different  $Re$  values, while figure 12(b) plots it for one  $Re$  but three  $Ca$  values. To understand the interaction phenomenon better, we simulate the dynamics of two drops in a shear. In figure 12(c), we plot the contributions to the interfacial stresses  $N_1^{int}$  and  $N_2^{int}$  due to one of them as well as the azimuthal angle between the drops as functions of time. As noted above, the angle is closer to  $180^\circ$  as the drops approach each other and  $0^\circ$  as they separate. The effects on the normal stress differences (increasing for  $N_1^{int}$  and decreasing for  $N_2^{int}$ ) are highest when the drops approach each other, and the opposite happens during separation. However, from the contact pair-distribution function (figure 12a),

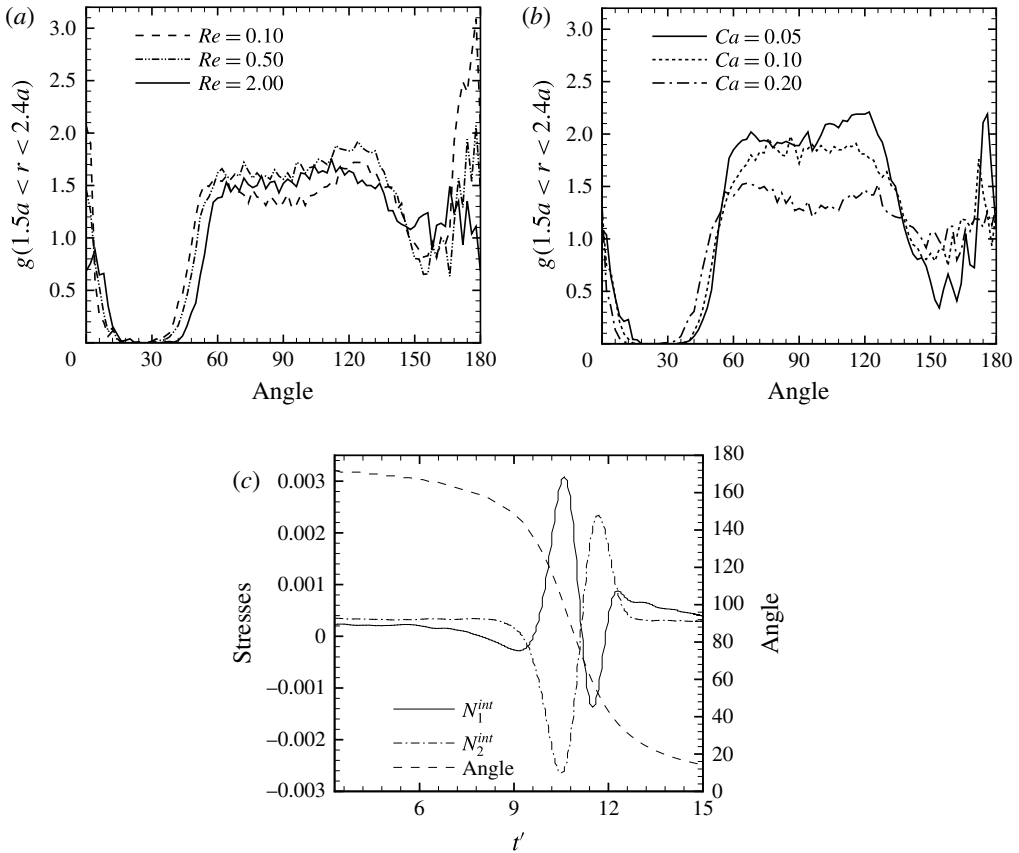


FIGURE 12. Pair distributions as a function of different relative orientations in the shear plane at  $\phi = 20\%$  (a) for different  $Re$  and  $Ca = 0.05$  and (b) for different  $Ca$  and  $Re = 1.0$ . (c) Time evolution of interfacial stresses (non-dimensionalized by  $\mu\dot{\gamma}$ ) arising from a single drop during pair interactions at  $Re = 1.0$  and  $Ca = 0.05$ .

we noted already that the probability is much higher in the compression quadrant. With increasing capillary number the peak value of the probability density in this quadrant decreases (figure 12b). The increase of  $N_1^{int}$  and decrease of  $N_2^{int}$  with volume fraction  $\phi$  can now be understood as resulting from increased probability of contact interactions between drops; the individual droplet stresslet contribution increases during close encounter in the compression quadrant. In figure 12(a), it can be noted that with increasing  $Re$ , the zero probability region moves closer to the extension axis, as was also observed for a rigid sphere suspension (Kulkarni & Morris 2008). However, that simulation for a rigid sphere suspension showed an increase in pair probability at  $0^\circ$  with increasing  $Re$ , indicating that spheres tend to line up along the flow direction. In contrast, here we see a decrease in the corresponding probability at  $0^\circ$  with increasing  $Re$ .

### 3.7. Perturbation stresses $\sigma^{ptb}$

Figure 13 shows the variation of the perturbation stress with various parameters. Three components,  $\sigma_{xx}^{ptb}$ ,  $\sigma_{yy}^{ptb}$  and  $\sigma_{zz}^{ptb}$ , are plotted in figure 13(a) as functions of the volume fraction for  $Ca = 0.05$  and  $Re = 1.0$ . The cross-components  $\sigma_{xy}^{ptb}$ ,  $\sigma_{zy}^{ptb}$

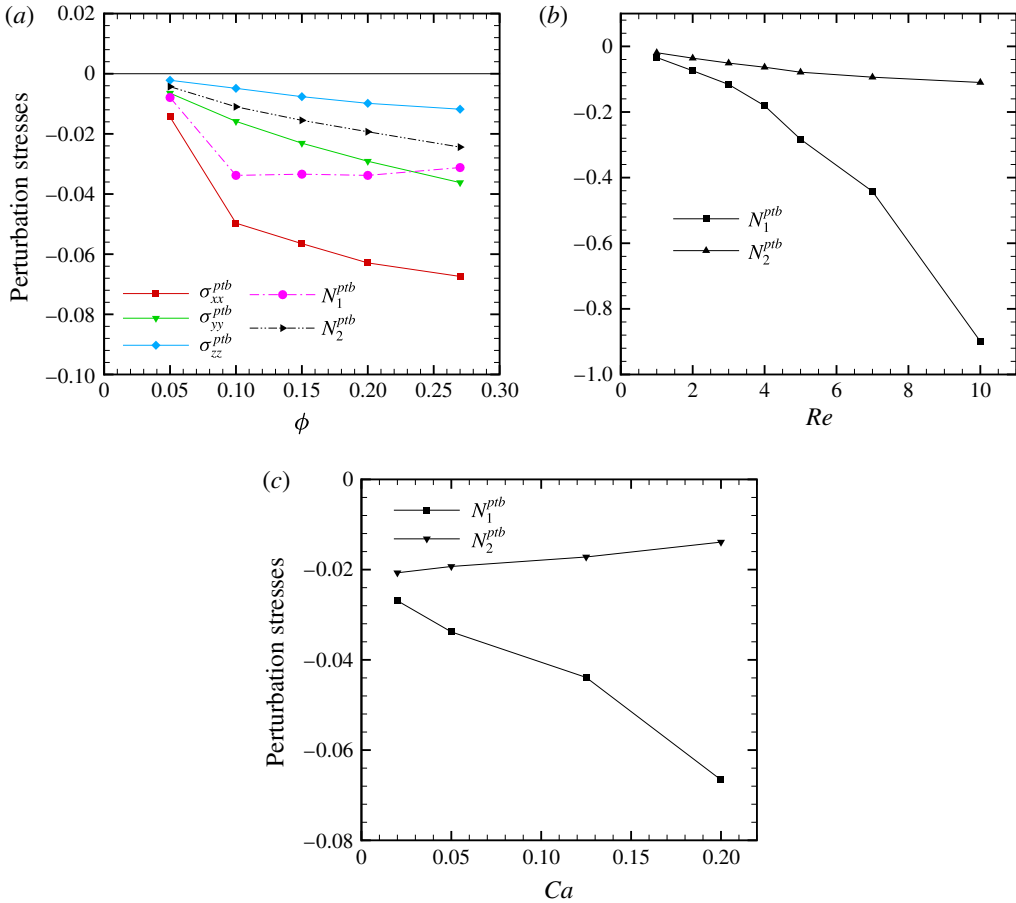


FIGURE 13. (Colour online) (a) Variation of the perturbation stresses (non-dimensionalized by  $\mu\dot{\gamma}$ ) with the volume fraction at  $Re = 1.0$  and  $Ca = 0.05$ . At a fixed volume fraction  $\phi = 20\%$ , variation of the perturbation stress differences with  $Re$  at  $Ca = 0.05$  (b), and with  $Ca$  at  $Re = 1.0$  (c).

and  $\sigma_{xz}^{ptb}$  are relatively small quantities and they do not affect the total stresses. They are therefore not plotted. The components  $\sigma_{yy}^{ptb}$  and  $\sigma_{zz}^{ptb}$  show a roughly linear dependence with volume fraction, and if the curves are extrapolated they will become zero at diminishing volume fraction. However,  $\sigma_{xx}^{ptb}$  shows a nonlinear dependence, as is evident from the fact that the curve has to pass through the origin. The same plot also shows the dependence of  $N_1^{ptb}$  and  $N_2^{ptb}$  on the volume fraction. It should be noted that with increasing volume fraction the magnitude of these perturbative normal stresses increases. Figure 13(b) shows the dependence of the perturbative normal stress differences with the Reynolds number at  $Ca = 0.05$  at a fixed volume fraction of 20%. It further shows that the perturbative normal stresses, although small in comparison to the interfacial stresses for small  $Re$  ( $Re < 1.0$ ), increase in magnitude sharply with increasing Reynolds number, making them eventually the dominant contribution in the total excess stress. Comparing with the interfacial contribution described in the previous subsection, we can note that the perturbative stresses become comparable to it at large Reynolds numbers for larger volume fractions –  $Re \sim 1$  for  $\phi = 10\%$ ,

$Re \sim 2$  for  $\phi = 20\%$  and  $Re \sim 4$  for  $\phi = 27\%$ . While  $N_2^{ptb}$  varies approximately linearly with  $Re$ ,  $N_1^{ptb}$  shows a weak nonlinear decrease with  $Re$  for larger  $Re$  values, as was also observed by Li & Sarkar (2005*b*) for dilute simulations. As the curves indicate, the perturbation stresses should vanish at zero  $Re$ . The linear scaling of the perturbation stress differences with Reynolds number (at least for the low Reynolds numbers) can be explained by noting that  $\mathbf{u}' \sim \dot{\gamma}a$  and the stresses are scaled by  $\mu\dot{\gamma}$ , leading to  $\sigma^{ptb}/\mu\dot{\gamma} \sim Re \int_V \rho \mathbf{u}'\mathbf{u}' dV$ .

Figure 13(c) shows the variation of the perturbation stress differences with the capillary number at a fixed Reynolds number of  $Re = 1.0$  and volume fraction of  $\phi = 0.20$ . Here,  $N_1^{ptb}$  shows a steep decrease with the capillary number. This is due to a steep decrease in  $\sigma_{xx}^{ptb}$  with  $Ca$  which is arising due to increase in the disturbances along the  $x$  direction (flow direction). This can be explained by the fact that increasing capillary number orients and deforms the drops more along the  $x$ -direction which in turn increases the disturbances along that axis.

### 3.8. Total excess stresses

The total effective stress characterizing the bulk properties of the emulsion contains the excess stress due to the presence of the dispersed phase. According to equation (2.3), for a viscosity-matched system such as the one considered here, the excess stress  $\sigma^{excess}$  consists of the interface contribution  $\sigma^{int}$  and the perturbation stress  $\sigma^{ptb}$  individually discussed in the previous sections. Figure 14(a–c) plots the excess stresses as functions of the Reynolds number for different volume fractions at  $Ca = 0.05$ . Because of the dominance of the interfacial contributions in the low- $Re$  region, the excess stresses show the same qualitative behaviour as the interfacial stresses in this range. The perturbative stresses make a negative contribution and the excess first normal stress difference remains negative for most  $Re$  values. Its variation with  $Re$  is steeper than that of the interfacial counterpart because of the large value of the perturbative contribution at  $Re > 1.0$ . On the other hand, the interfacial second normal stress difference is largely positive. A negative contribution of the perturbative stress makes the curve of the excess second normal stress difference flatter. Compared with the interfacial shear stress the perturbative stress is much smaller in magnitude and therefore the excess shear stress remains almost the same. As noted before, even after scaling by the volume fraction  $\phi$ , the excess stresses for different values of  $\phi$  do not collapse, indicating a nonlinear dependence. Figure 14(d) plots the excess stresses as a function of the volume fraction along with an approximate quadratic fit:

$$\left. \begin{aligned} N_1^{excess}/\mu\dot{\gamma} &= \phi(-0.4815 + 4.681\phi), \\ N_2^{excess}/\mu\dot{\gamma} &= \phi(0.1396 - 1.805\phi), \\ \Sigma_{xy}^{excess}/\mu\dot{\gamma} &= \phi(2.01 + 2.687\phi). \end{aligned} \right\} \quad (3.6)$$

In figure 15(a–c), we plot the excess first and second normal stress differences as well as the shear stress as functions of the Reynolds number for different capillary numbers. Figures 14(a–c) and 15(a–c) show approximately linear dependence with  $Re$  at least for the smaller range of  $0.1 \leq Re \leq 5$ . In figure 15(d), we show that the excess stresses approximately follow a quadratic variation with capillary number:

$$\left. \begin{aligned} N_1^{excess}/\mu\dot{\gamma} &= -0.0448 + 3.008Ca - 2.764Ca^2, \\ N_2^{excess}/\mu\dot{\gamma} &= -0.1055 - 0.9591Ca + 1.414Ca^2, \\ \Sigma_{xy}^{excess}/\mu\dot{\gamma} &= 0.6044 - 1.615Ca + 3.113Ca^2. \end{aligned} \right\} \quad (3.7)$$

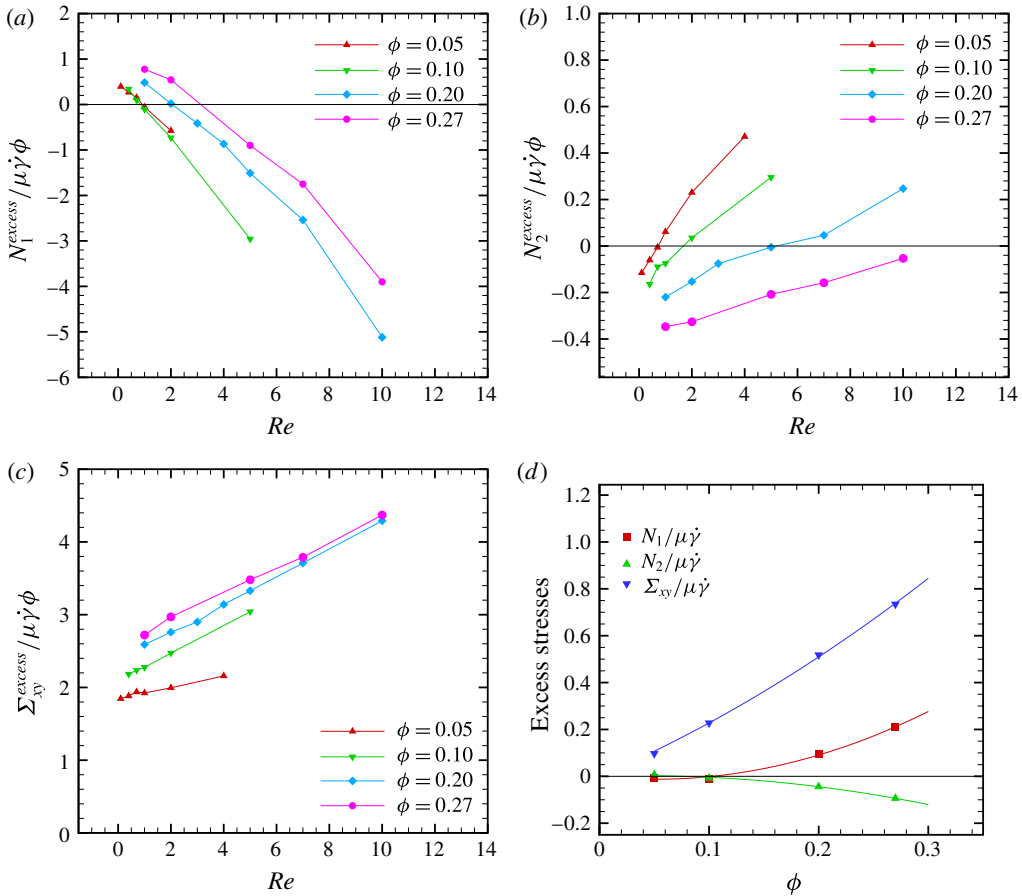


FIGURE 14. (Colour online) Excess stresses with  $Re$  for different volume fractions at  $Ca=0.05$ : (a)  $N_1^{excess}$ , (b)  $N_2^{excess}$  and (c)  $\Sigma_{xy}^{excess}$ . (d) Excess stresses versus  $\phi$  along with a fit at  $Re = 1.0$  and  $Ca = 0.05$ .

It should be noted that the viscoelastic stresses (e.g. the first normal stress difference) arising from deforming drops are quite comparable to the viscous stresses at higher  $Ca$  values ( $Ca \sim 0.2$ ), as can be seen in figure 15(d). By direct numerical simulation, as used here, one can develop useful general phenomenological correlations between the effective rheological stresses and the relevant non-dimensional parameters. However, robust accurate correlations in the entire range of capillary number, Reynolds number and volume fraction require extensive numerical simulations varying all three parameters. The primary goal of this paper is to elucidate the underlying physics of the excess stress, and therefore such a computational endeavour remains outside the scope of this paper. Finally, to elucidate the effect of the sign change of the normal stress differences, we note that a positive  $N_1$  in a polymeric flow exerts a compressive stress on the bottom plate while being sheared in a cone and plate rheometer in a Stokes flow, in contrast to zero force for a Newtonian fluid. The inertia induced sign change demonstrated in this paper (figures 14 and 15) indicates that even a small amount of inertia (drop Reynolds number 2–5) is sufficient to change the physics, giving rise to tensile force on the bottom plate.

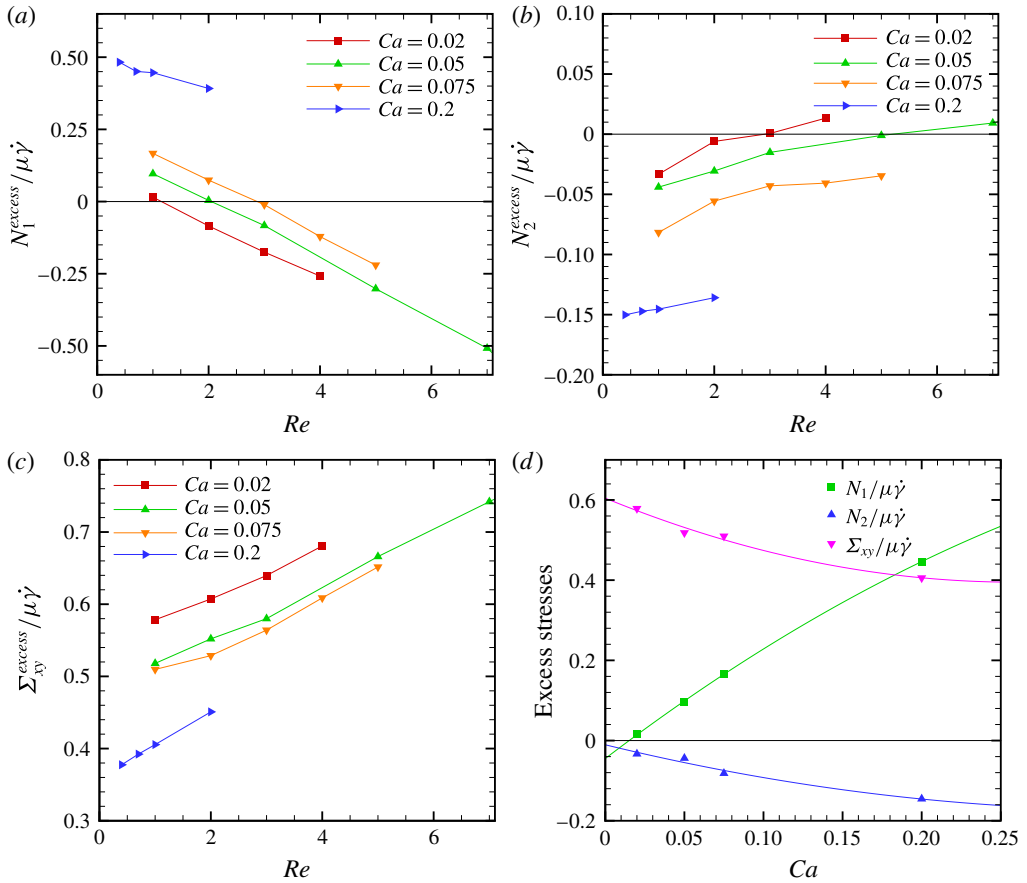


FIGURE 15. (Colour online) Excess stresses with  $Re$  for different capillary numbers at  $\phi = 20\%$ : (a)  $N_1^{excess}$ , (b)  $N_2^{excess}$  and (c)  $\Sigma_{xy}^{excess}$ . (d) Excess stresses versus  $Ca$  along with a fit at  $Re = 1.0$  and  $\phi = 20\%$ .

#### 4. Summary and conclusion

Dense emulsions of viscous drops in plane shear are simulated using direct numerical simulation in the presence of finite inertia, and the effective rheology of such emulsions is computed. Previously, we have shown that finite inertia can induce a sign change of the effective first and second normal stress differences. The results were obtained in the dilute limit, where drop–drop interactions were ignored – the results were purely based on a single-drop simulation. Here, the same phenomenon is investigated by simulating an equiviscous multidrop system and extended to dense emulsion – with volume fraction up to 27%.

The Batchelor formulation is used for the stress computation, which indicates two distinct components for the viscosity-matched system considered here – purely geometric interfacial stresses determined by the drop shapes and perturbative Reynolds type stresses due to inertia. Both components are investigated, varying the volume fraction, capillary number and Reynolds number. Previously, in the dilute limit (Li & Sarkar 2005b), we found that the interfacial stresses dominate over the perturbative component at small Reynolds number. Here, we find that the magnitude of the

perturbative stresses increases with the volume fraction and even more sharply with the Reynolds number, eventually making it the dominant contribution at higher  $Re$  values. Our results compare well with those obtained by Stokes flow boundary element simulation (except for small differences at low capillary numbers with Zinchenko & Davis (2002)) and an experimentally obtained empirical relation for effective viscosity as a function of volume fraction. In the dilute limit, we recover the single-drop result obtained earlier. The sign change at finite inertia stems from drops getting aligned at more than  $45^\circ$  with the flow direction. A physical explanation is provided as to how this causes a decrease (increase) in the interfacial first (second) normal stress difference with increasing Reynolds number, eventually making it negative (positive). The increasing inclination angle and drop deformation are also shown to cause the observed increase in effective shear stress. In a dense emulsion, the drop–drop interactions cause the drops to align more with the flow, lessening the above effects. With increasing capillary number, the interfacial first normal stress difference increases but the second normal stress difference and shear stress decrease due to increased drop deformation and enhanced drop alignment with the flow.

Unlike the dilute emulsion result, the effective stresses are not linear in the volume fraction. The effects of drop–drop interactions are investigated by examining the contact pair-distribution function, which experiences an increase when the drops are interacting in the compression quadrant. The close interaction causes a sharp increase in the drop contributions to the interfacial normal stress differences – positive for the first and negative for the second – delaying the sign change to higher Reynolds numbers. The perturbative Reynolds stresses show linear decrease with Reynolds number for small Reynolds numbers – the approximate linear scaling can be explained on dimensional grounds. With increasing capillary number, the perturbative first normal stress shows a steep decrease due to increased deformation and flow alignment. The excess stresses also show approximately linear scaling with the Reynolds number at least for the low-Reynolds-number range  $0.1 \leq Re \leq 5$ . A quadratic fit of the excess stresses with the volume fraction  $\phi$  is obtained in the range considered.

### Acknowledgements

This work is partially supported by NSF grants no. CBET-1205322, DMR-1239105. The authors acknowledge H. Haddadi who graciously shared his code for computation of the pair-distribution function.

### REFERENCES

- AGGARWAL, N. & SARKAR, K. 2007 Deformation and breakup of a viscoelastic drop in a Newtonian matrix under steady shear. *J. Fluid Mech.* **584**, 1–21.
- AGGARWAL, N. & SARKAR, K. 2008a Effects of matrix viscoelasticity on viscous and viscoelastic drop deformation in a shear flow. *J. Fluid Mech.* **601**, 63–84.
- AGGARWAL, N. & SARKAR, K. 2008b Rheology of an emulsion of viscoelastic drops in steady shear. *J. Non-Newtonian Fluid Mech.* **150**, 19–31.
- ALMUSALLAM, A. S., LARSON, R. G. & SOLOMON, M. J. 2000 A constitutive model for the prediction of ellipsoidal droplet shapes and stresses in immiscible blends. *J. Rheol.* **44**, 1055–1083.
- BATCHELOR, G. & GREEN, J. 1972 The determination of the bulk stress in a suspension of spherical particles to order  $c^2$ . *J. Fluid Mech.* **56**, 401–427.

- BATCHELOR, G. K. 1970 Stress system in a suspension of force-free particles. *J. Fluid Mech.* **41**, 545–570.
- BRACKBILL, J. U., KOTHE, D. B. & ZEMACH, C. 1992 A continuum method for modeling surface-tension. *J. Comput. Phys.* **100**, 335–354.
- BRADY, J. F. & BOSSIS, G. 1988 Stokesian dynamics. *Annu. Rev. Fluid Mech.* **20**, 111–157.
- BRADY, J. F. & MORRIS, J. F. 1997 Microstructure of strongly sheared suspensions and its impact on rheology and diffusion. *J. Fluid Mech.* **348**, 103–139.
- BUNNER, B. & TRYGGVASON, G. 1999 Direct numerical simulations of three-dimensional bubbly flows. *Phys. Fluids* **11**, 1967–1969.
- CHAN, P. C. H. & LEAL, L. G. 1981 An experimental study of drop migration in shear flow between concentric cylinders. *Intl J. Multiphase Flow* **7**, 83–99.
- CHOI, S. J. & SCHOWALTER, W. R. 1975 Rheological properties of non-dilute suspensions of deformable particles. *Phys. Fluids* **18**, 420–427.
- CLAUSEN, J. R., REASOR, D. A. & AIDUN, C. K. 2011 The rheology and microstructure of concentrated non-colloidal suspensions of deformable capsules. *J. Fluid Mech.* **685**, 202–234.
- DOI, M. & OHTA, T. 1991 Dynamics and rheology of complex interfaces. I. *J. Chem. Phys.* **95**, 1242–1248.
- EINSTEIN, A. 1906 Eine neue Bestimmung der Molekul-dimension. *Ann. Phys.* **19**, 289–306.
- FOSS, D. R. & BRADY, J. F. 2000 Structure, diffusion and rheology of Brownian suspensions by Stokesian dynamics simulation. *J. Fluid Mech.* **407**, 167–200.
- FRANKEL, N. A. & ACRIVOS, A. 1970 Constitutive equation for a dilute emulsion. *J. Fluid Mech.* **44**, 65.
- HADDADI, H. & MORRIS, J. F. 2014 Microstructure and rheology of finite inertia neutrally buoyant suspensions. *J. Fluid Mech.* **749**, 431–459.
- HAN, C. D. & KING, R. G. 1980 Measurement of the rheological properties of concentrated emulsions. *J. Rheol.* **24**, 213–237.
- JACKSON, N. E. & TUCKER, C. L. 2003 A model for large deformation of an ellipsoidal droplet with interfacial tension. *J. Rheol.* **47**, 659–682.
- KULKARNI, P. M. & MORRIS, J. F. 2008 Suspension properties at finite Reynolds number from simulated shear flow. *Phys. Fluids* **20**, 040602.
- LARSON, R. G. 1999 *The Structure and Rheology of Complex Fluids*. Oxford University Press.
- LEE, H. M. & PARK, O. O. 1994 Rheology and dynamics of immiscible polymer blends. *J. Rheol.* **38**, 1405–1425.
- LI, X. Y. & SARKAR, K. 2005a Drop dynamics in an oscillating extensional flow at finite Reynolds numbers. *Phys. Fluids* **17**, 027103.
- LI, X. Y. & SARKAR, K. 2005b Effects of inertia on the rheology of a dilute emulsion of drops in shear. *J. Rheol.* **49**, 1377–1394.
- LI, X. Y. & SARKAR, K. 2005c Negative normal stress elasticity of emulsions of viscous drops at finite inertia. *Phys. Rev. Lett.* **95**.
- LI, X. Y. & SARKAR, K. 2005d Numerical investigation of the rheology of a dilute emulsion of drops in an oscillating extensional flow. *J. Non-Newtonian Fluid Mech.* **128**, 71–82.
- LI, X. Y. & SARKAR, K. 2006 Drop deformation and breakup in a vortex at finite inertia. *J. Fluid Mech.* **564**, 1–23.
- LI, X. Y. & SARKAR, K. 2008 Front tracking simulation of deformation and buckling instability of a liquid capsule enclosed by an elastic membrane. *J. Comput. Phys.* **227**, 4998–5018.
- LIN, C.-J., PEERY, J. H. & SHOWALTER, W. R. 1970 Simple shear flow round inertial effects and suspension rheology. *J. Fluid Mech.* **44**, 1–17.
- LOEWENBERG, M. & HINCH, E. J. 1996 Numerical simulation of a concentrated emulsion in shear flow. *J. Fluid Mech.* **321**, 395–419.
- LOEWENBERG, M. & HINCH, E. J. 1997 Collision of two deformable drops in shear flow. *J. Fluid Mech.* **338**, 299–315.
- MAFFETTONE, P. L. & MINALE, M. 1998 Equation of change for ellipsoidal drops in viscous flow. *J. Non-Newtonian Fluid Mech.* **78**, 227–241.

- MORRIS, J. F. & KATYAL, B. 2002 Microstructure from simulated Brownian suspension flows at large shear rate. *Phys. Fluids* **14**, 1920.
- MUKHERJEE, S. & SARKAR, K. 2010 Effects of viscoelasticity on the retraction of a sheared drop. *J. Non-Newtonian Fluid Mech.* **165**, 340–349.
- MUKHERJEE, S. & SARKAR, K. 2011 Viscoelastic drop falling through a viscous medium. *Phys. Fluids* **23**, 013101.
- MUKHERJEE, S. & SARKAR, K. 2013 Effects of matrix viscoelasticity on the lateral migration of a deformable drop in a wall-bounded shear. *J. Fluid Mech.* **727**, 318–345.
- MUKHERJEE, S. & SARKAR, K. 2014 Lateral migration of a viscoelastic drop in a Newtonian fluid in a shear flow near a wall. *Phys. Fluids* **26**, 103102.
- OLAPADE, P. O., SINGH, R. K. & SARKAR, K. 2009 Pair-wise interactions between deformable drops in free shear at finite inertia. *Phys. Fluids* **21**, 063302.
- OLDROYD, J. G. 1953 The elastic and viscous properties of emulsions and suspensions. *Proc. R. Soc. Lond. A* **218**, 122–132.
- PAL, R. 2003 Viscous behavior of concentrated emulsions of two immiscible Newtonian fluids with interfacial tension. *J. Colloid Interface Sci.* **263**, 296–305.
- PATANKAR, N. A. & HU, H. H. 2002 Finite Reynolds number effect on the rheology of a dilute suspension of neutrally buoyant circular particles in a Newtonian fluid. *Intl J. Multiphase Flow* **28**, 409–425.
- PETERS, G. W. M., HANSEN, S. & MEIJER, H. E. H. 2001 Constitutive modeling of dispersive mixtures. *J. Rheol.* **45**, 659–689.
- PHUNG, T. N., BRADY, J. F. & BOSSIS, G. 1996 Stokesian dynamics simulation of Brownian suspensions. *J. Fluid Mech.* **313**, 181–207.
- RAISKINMAKI, P., ASTROM, J. A., KATAJA, M., LATVA-KOKKO, M., KOPONEN, A., JASBERG, A., SHAKIB-MANESH, A. & TIMONEN, J. 2003 Clustering and viscosity in a shear flow of a particulate suspension. *Phys. Rev. E* **68**, 5.
- RAJA, R. V., SUBRAMANIAN, G. & KOCH, D. L. 2010 Inertial effects on the rheology of a dilute emulsion. *J. Fluid Mech.* **646**, 255–296.
- SARKAR, K. & SCHOWALTER, W. R. 2000 Deformation of a two-dimensional viscoelastic drop at non-zero Reynolds number in time-periodic extensional flows. *J. Non-Newtonian Fluid Mech.* **95**, 315–342.
- SARKAR, K. & SCHOWALTER, W. R. 2001 Deformation of a two-dimensional drop at non-zero Reynolds number in time-periodic extensional flows: numerical simulation. *J. Fluid Mech.* **436**, 177–206.
- SCHOWALTER, W. R., CHAFFEY, C. E. & BRENNER, H. 1968 Rheological behavior of a dilute emulsion. *J. Colloid Interface Sci.* **26**, 152.
- SIBILLO, V., PASQUARIELLO, G., SIMEONE, M., CRISTINI, V. & GUIDO, S. 2006 Drop deformation in microconfined shear flow. *Phys. Rev. Lett.* **97**, 054502.
- SINGH, R. K., LI, X. Y. & SARKAR, K. 2014 Lateral migration of a capsule in plane shear near a wall. *J. Fluid Mech.* **739**, 421–443.
- SINGH, R. K. & SARKAR, K. 2009 Effects of viscosity ratio and three dimensional positioning on hydrodynamic interactions between two viscous drops in a shear flow at finite inertia. *Phys. Fluids* **21**, 103303.
- SINGH, R. K. & SARKAR, K. 2011 Inertial effects on the dynamics, streamline topology and interfacial stresses due to a drop in shear. *J. Fluid Mech.* **683**, 149–171.
- SMART, J. R. & LEIGHTON, J. D. T. 1991 Measurement of the drift of a droplet due to the presence of a plane. *Phys. Fluids A* **3**, 21–28.
- SUBRAMANIAN, G., KOCH, D. L., ZHANG, J. S. & YANG, C. 2011 The influence of the inertially dominated outer region on the rheology of a dilute dispersion of low-Reynolds-number drops or rigid particles. *J. Fluid Mech.* **674**, 307–358.
- TAKAHASHI, Y., KURASHIMA, N., NODA, I. & DOI, M. 1994 Experimental tests of the scaling relation for textured materials in mixtures of 2 immiscible fluids. *J. Rheol.* **38**, 699–712.
- TAYLOR, G. I. 1932 The viscosity of a fluid containing small drops of another fluid. *Proc. R. Soc. Lond. A* **138**, 41–48.

- TUCKER, C. L. & MOLDENAERS, P. 2002 Microstructural evolution in polymer blends. *Annu. Rev. Fluid Mech.* **34**, 177–210.
- VINCKIER, I., MOLDENAERS, P. & MEWIS, J. 1996 Relationship between rheology and morphology of model blends in steady shear flow. *J. Rheol.* **40**, 613–631.
- WETZEL, E. D. & TUCKER, C. L. 2001 Droplet deformation in dispersions with unequal viscosities and zero interfacial tension. *J. Fluid Mech.* **426**, 199–228.
- ZHOU, H. & POZRIKIDIS, C. 1993 The flow of ordered and random suspensions of two-dimensional drops in a channel. *J. Fluid Mech.* **255**, 103–127.
- ZINCHENKO, A. Z. & DAVIS, R. H. 2000 An efficient algorithm for hydrodynamical interaction of many deformable drops. *J. Comput. Phys.* **157**, 539–587.
- ZINCHENKO, A. Z. & DAVIS, R. H. 2002 Shear flow of highly concentrated emulsions of deformable drops by numerical simulations. *J. Fluid Mech.* **455**, 21–62.
- ZINCHENKO, A. Z. & DAVIS, R. H. 2004 Hydrodynamical interaction of deformable drops. In *Emulsions: Structure Stability and Interactions* (ed. D. N. Petsev), chap. 10, pp. 391–447. Elsevier.
- ZINCHENKO, A. Z. & DAVIS, R. H. 2015 Extensional and shear flows, and general rheology of concentrated emulsions of deformable drops. *J. Fluid Mech.* **779**, 197–244.